

An efficient solid shell material point method for large deformation of thin structures

Jiasheng Li | Ruichen Ni | Zhixin Zeng | Xiong Zhang[✉]

School of Aerospace Engineering,
Tsinghua University, Beijing,
People's Republic of China

Correspondence

Xiong Zhang, School of Aerospace
Engineering, Tsinghua University, Beijing
100084, People's Republic of China.
Email: xzhang@tsinghua.edu.cn

Funding information

National Natural Science Foundation of
China, Grant/Award Number: 12172192

Abstract

The standard material point method (MPM) encounters severe numerical difficulties in simulating shell structures. In order to overcome the shortcomings of locking effects, the discretization size of background grid should be small enough, usually smaller than 1/5 of the shell thickness, which however will lead to prohibitive computational cost. A novel solid shell material point method (SSMPM) is proposed to efficiently model the large deformation of thin structures. The SSMPM describes the material domain of shell structures by shell particles with hexahedral particle domains. The locking treatments of solid shell element are then introduced in SSMPM, which results in the correction of strain field throughout the shell thickness. Namely, the assumed natural strain (ANS) method is adopted to eliminate the shear locking and trapezoidal locking, while the enhanced assumed strain (EAS) method is employed to eliminate the thickness locking. With the precise description of bending modes, a single layer of particles and a coarse background grid could be used in shell structure simulations with the SSMPM, which dramatically increases the computational efficiency. A local multi-mesh contact method is presented to naturally couple SSMPM and MPM for the contact situations of shells with other objects. Several numerical examples, including beam vibration, pinched cylinder with free edges and full hemispherical shell, are performed to verify and validate the SSMPM, which shows that the SSMPM considerably outperforms the standard MPM in these situations. A fluid–structure interaction problem and the penetration of a thin plate are investigated based on the contact method and the results are in good agreement with those in the literature.

KEYWORDS

assumed natural strain, enhanced assumed strain, locking, material point method, solid shell

1 | INTRODUCTION

Shell structures have a wide range of applications in engineering practice, and always play a significant role in large-span situations, such as the wings of airplanes and the hulls of ships. For safety and security, large deformation and destruction of shell structures under extreme load conditions have attracted great attention. With the large span of shell structures and inhomogeneous material distribution, experiments of equal proportion are ordinarily expensive, while the

results corresponding to scaled models under the same experimental conditions may vary from each other. Therefore, the development of efficient and powerful algorithms to simulate complicated responses of shell structures remains an active field of research.

Solid shell elements¹⁻¹⁰ in finite element method (FEM) have been successfully applied in the moderate and mild deformation of shell structures. However when simulating extreme deformation and fragmentation of shell structures, traditional mesh-based methods suffer from mesh distortion and violate the law of mass conservation with erosion algorithms, while mesh-free methods demonstrate outstanding advantages. As a typical representative of mesh-free methods, the material point method (MPM)^{11,12} adopts a set of Lagrangian particles moving through Eulerian background grid to surmount the challenges in simulations of extreme deformation. The MPM has shown its success in simulating various kinds of extreme deformation events during these decades, such as hyper velocity impact,¹³⁻¹⁶ penetration,^{17,18} fracture evolution¹⁹⁻²² and fluid–structure interaction.²³⁻²⁶ And plenty of variants have been proposed to improve the accuracy and stability of MPM.²⁷⁻³³ Bardenhagen et al.²⁷ developed the generalized interpolation material point (GIMP) method by accounting for spatial volume of each particle to reduce the cell crossing noise caused by the discontinuity in the gradient of linear shape function. Sadeghirad et al.³¹ presented the convected particle domain interpolation (CPDI) method with parallelogram particle domains to track the material motion, which is more accurate and efficient than GIMP. And the particle domains have been further extended to quadrilaterals in 2-D (hexahedra in 3-D) by tracking their corner positions in the second-order convected particle domain interpolation (CPDI2) method.³² Steffen et al.²⁹ adopted smoother basis functions including the quadratic and cubic B-spline as background grid basis function to decrease the integration errors. Liang et al.³³ proposed the staggered grid material point (SGMP) method with the volume integrals in the weak form evaluated by cell center quadrature instead of particle quadrature to eliminate the cell crossing noise.

Formulations for shell structures have been established in various mesh-free methods, such as the smoothed particle hydrodynamics (SPH),^{34,35} element-free Galerkin (EFG) method,³⁶⁻³⁸ reproducing kernel particle method (RKPM)³⁹⁻⁴² and peridynamics (PD).^{43,44} Krysl and Belytschko³⁷ introduced the Kirchhoff–Love theory in EFG method to carry out the static analysis of thin shells, where the C^1 continuity was easily achieved by moving least-squares approximation. Wang and Chen³⁸ proposed a meshfree Mindlin–Reissner plate formulation and eliminated the shear locking by imposing Kirchhoff mode reproducing conditions. For the dynamic responses, Maurel and Combescure³⁵ presented a SPH shell formulation based on the Mindlin–Reissner’s thick shell theory for the simulation of shell fracture under impact. Peng et al. introduced the shell formulation in RKPM for the large deformation of curved shells⁴¹ and further studied the dynamic fracture.⁴² It is attractive that these formulations can discretize shell structures with a single layer of particles and can be implemented naturally in the framework of corresponding mesh-free methods.

The standard MPM has been used to simulate beam and shell structures in different situations.⁴⁵⁻⁴⁹ With both explicit and implicit MPM, Chen et al.⁴⁶ investigated the vibration of a cantilever beam. De Vaucorbeil and Nguyen⁴⁷ employed the total Lagrangian MPM to simulate a collision with large deformation of two hollow cylindrical shells. Ni et al.⁴⁹ applied MPM to study the fragmentation of a cylindrical shell under blast loading. Although satisfactory results were obtained by the MPM in their simulations, the discretization size of background grid was all taken as 1/8 of the shell thickness, which would lead to prohibitive computational cost. Several locking phenomena induced by the trilinear shape function will result in an overestimation of stress state and an underestimation of deformation when adopting a coarse background grid. And thus, the discretization size of background grid should be small enough for shell simulations with the standard MPM, usually smaller than 1/5 of the shell thickness.⁵⁰ Similar to the standard MPM, the CPDI2 also needs a fine background grid for shell structures. In order to obtain an accurate result of a cantilever beam, Nguyen et al.⁵¹ set the size of grid cell as 1/8 of the thickness in CPDI-T4 which is a version of CPDI2 with tetrahedral particle domains. However to our best knowledge, there is a handful of literature about MPM shell formulations which can effectively surmount these numerical difficulties. Guo et al.⁵² combined MPM and subdivision finite elements for thin-shell simulations with frictional contact, which provided a powerful tool for contact scenarios. With the Kirchhoff–Love theory, C^1 continuous interpolating functions were required over the shell mid-surface and the range of applications was limited to thin shells. Kang et al.⁵³ presented a MPM beam formulation by introducing the rotational degrees of freedom (DOFs) for dynamic responses under frictional contacts, which so far has not been extended to a shell formulation.

A novel solid shell material point method (SSMPM) is put forward in this paper by introducing solid shell formulation, which incorporates the bending modes of solid shell element in the MPM. The SSMPM describes the material domain of shell structures by shell particles with hexahedral particle domains. The locking treatments of solid shell

element are then introduced in SSMPM, which results in the correction of strain field throughout the shell thickness. The assumed natural strain (ANS) method^{54,55} is adopted to eliminate the shear locking and trapezoidal locking,^{56,57} while the enhanced assumed strain (EAS) method^{58,59} is employed to eliminate the thickness locking. With the precise description of bending modes, a coarse background grid could be used in shell structure simulations with SSMPM, which dramatically increases the computational efficiency. The SSMPM and MPM share the same nodal DOFs, so that the local multi-mesh contact method^{18,60} is presented to naturally couple them for the contact situations of shells with other objects. Furthermore, adaptively converting the SSMPM shell particles into the standard MPM particles is readily, which makes SSMPM a promising method to simulate the extreme deformation and fragmentation of shell structures. Several numerical examples, including pinched cylinder with end diaphragms, beam vibration, pinched cylinder with free edges and full hemispherical shell are performed to verify and validate the proposed method, and numerical results show that the SSMPM considerably outperforms the standard MPM in these situations. A fluid–structure interaction problem and the penetration of a thin plate are investigated based on the contact method and the results are in good agreement with those in the literature.

The rest of this article is organized as follows. In Section 2, the basic idea of MPM and its shortcomings in shell simulations are briefly reviewed. Then, Section 3 presents the detailed methodology of the proposed SSMPM in terms of the shell particle and locking treatments. And a local multi-mesh contact method for coupling SSMPM and MPM is presented in Section 4. The algorithm summary and remark of SSMPM are given in Section 5. Validations and benchmark simulations are presented in Section 6. Finally Section 7 gives the conclusion.

2 | MATERIAL POINT METHOD

The weak form equivalent to momentum equations and traction boundary condition in updated Lagrangian formulation is given as

$$\int_{\Omega} \rho \ddot{\mathbf{u}} \cdot \delta \mathbf{u} dV + \int_{\Omega} \boldsymbol{\sigma} : \delta \boldsymbol{\varepsilon} dV - \int_{\Omega} \rho \mathbf{b} \cdot \delta \mathbf{u} dV - \int_{\Gamma_t} \bar{\mathbf{t}} \cdot \delta \mathbf{u} dA = 0, \quad (1)$$

where Γ_t denotes the traction boundary of material domain Ω , ρ is the current density, \mathbf{u} is the displacement, $\delta \mathbf{u}$ is the virtual displacement, $\boldsymbol{\sigma}$ is the Cauchy stress in the current configuration, $\boldsymbol{\varepsilon}$ is the Cauchy strain, \mathbf{b} is the body force per unit mass and $\bar{\mathbf{t}}$ is the traction on the boundary.

2.1 | Standard MPM

The standard MPM adopts Lagrangian particles and an Eulerian background grid for spatial discretization. And leapfrog central difference integration scheme can be used for temporal discretization in the explicit MPM. Its computational process in each time step consists of four steps: (1) particle-to-grid projection, (2) background grid momentum updating, (3) grid-to-particle mapping and particle updating, and (4) resetting the background grid.

2.1.1 | Spatial discretization

The standard MPM discretizes the material domain Ω into a set of Lagrangian particles moving through an Eulerian background grid, as shown in Figure 1. The particles act as quadrature points in calculating the integration of weak form equation, and material density can be given by

$$\rho(\mathbf{x}) = \sum_{p=1}^{n_p} m_p \delta(\mathbf{x} - \mathbf{x}_p), \quad (2)$$

where the subscript p denotes the variables associated with particle p , n_p is the total number of particles, m_p is the mass of particle p , δ is the Dirac delta function with dimension of the inverse of particle volume, \mathbf{x} is the spatial coordinates in the current configuration, and \mathbf{x}_p is the coordinates of particle p .

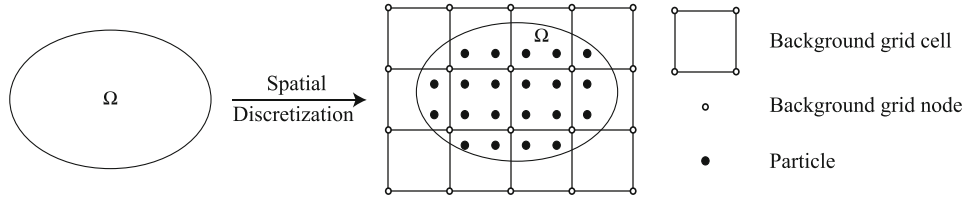


FIGURE 1 Spatial discretization of the standard MPM.

The displacement field $\mathbf{u}(\mathbf{x})$ of the computational domain is interpolated from the grid nodal displacement \mathbf{u}_I by the shape function $N_I(\mathbf{x})$ of each grid node I , namely

$$\mathbf{u}(\mathbf{x}) = \sum_{I=1}^{n_g} N_I(\mathbf{x}) \mathbf{u}_I, \quad (3)$$

where the subscript I denotes the variables associated with the grid node I , n_g is the total number of background grid nodes, $N_I(\mathbf{x})$ is the linear/bilinear/trilinear shape function in 1D/2D/3D as that used in the FEM.

Substituting Equations (2) and (3) into the weak form Equation (1) and invoking the arbitrariness of the virtual displacement $\delta \mathbf{u}_I$ lead to the discretized momentum equations at each grid node

$$\dot{\mathbf{p}}_I = \mathbf{f}_I^{\text{int}} + \mathbf{f}_I^{\text{ext}}, \quad \forall \mathbf{x}_I \notin \Gamma_u \quad (4)$$

in which Γ_u is the displacement boundary of the material domain,

$$\mathbf{p}_I = m_I \dot{\mathbf{u}}_I \quad (5)$$

is the momentum at grid node I ,

$$m_I = \sum_{p=1}^{n_p} m_p N_I(\mathbf{x}_p) \quad (6)$$

is the lumped grid mass matrix,

$$\mathbf{f}_I^{\text{int}} = - \sum_{p=1}^{n_p} \nabla N_{Ip} \cdot \boldsymbol{\sigma}_p V_p \quad (7)$$

and

$$\mathbf{f}_I^{\text{ext}} = \sum_{p=1}^{n_p} m_p N_{Ip} \mathbf{b}_p + \sum_{p=1}^{n_p} N_{Ip} \bar{\mathbf{t}}_p h^{-1} V_p \quad (8)$$

are the internal and external nodal forces, respectively. In Equation (7), $N_{Ip} = N_I(\mathbf{x}_p)$ is the shape function of the node I evaluated at the position of particle p , $\boldsymbol{\sigma}_p$ is the stress of particle p and V_p is the volume of particle p . In Equation (8), \mathbf{b}_p is the body force per unit mass of particle p , $\bar{\mathbf{t}}_p$ is the traction of particle p and h is the thickness of the fictitious layer used to convert the surface integral into a volume integral. Here, the strain rate $\dot{\boldsymbol{\epsilon}}_p$ and vorticity rate $\dot{\boldsymbol{\Omega}}_p$ for calculating $\boldsymbol{\sigma}_p$ are given as

$$\dot{\boldsymbol{\epsilon}}_p = \frac{1}{2} (\mathbf{v}_I \otimes \nabla N_{Ip} + \nabla N_{Ip} \otimes \mathbf{v}_I), \quad (9)$$

$$\dot{\boldsymbol{\Omega}}_p = \frac{1}{2} (\mathbf{v}_I \otimes \nabla N_{Ip} - \nabla N_{Ip} \otimes \mathbf{v}_I), \quad (10)$$

where \mathbf{v}_I is the grid nodal velocity.

2.1.2 | Temporal discretization

The leapfrog central difference integration scheme⁶¹ is used in the present work. The velocity $\mathbf{v}_I^{n+1/2}$ at time $t^{n+1/2}$ and the displacement \mathbf{u}_I^{n+1} at time t^{n+1} can be updated as

$$\mathbf{v}_I^{n+1/2} = \mathbf{v}_I^{n-1/2} + \mathbf{a}_I^n \Delta t^n, \quad (11)$$

$$\mathbf{u}_I^{n+1} = \mathbf{u}_I^n + \mathbf{v}_I^{n+1/2} \Delta t^{n+1/2}, \quad (12)$$

where

$$\Delta t^n = \frac{1}{2} (\Delta t^{n-1/2} + \Delta t^{n+1/2}) \quad (13)$$

is the time step at time t^n and $\Delta t^{n+1/2} = t^{n+1} - t^n$, and \mathbf{a}_I^n is the acceleration at time t^n calculated by Equation (4). For the stability requirement of central difference method, the critical time step¹² is given as

$$\Delta t_{\text{cr}} = \frac{d_g}{\max_p (c_p + |\mathbf{v}_p|)}, \quad (14)$$

where d_g is the grid cell size, c_p is the sound speed of particle p and \mathbf{v}_p is the velocity of particle p .

After updating the background grid momentum, physical variables of particles are updated by grid-to-particle mapping

$$\mathbf{v}_p^{n+1/2} = \mathbf{v}_p^{n-1/2} + \sum_{I=1}^{n_g} N_{Ip} \mathbf{a}_I^n \Delta t^n, \quad (15)$$

$$\mathbf{x}_p^{n+1} = \mathbf{x}_p^n + \sum_{I=1}^{n_g} N_{Ip} \mathbf{v}_I^{n+1/2} \Delta t^{n+1/2}, \quad (16)$$

The process of updating the stress can be carried out at the beginning of each time step or at the end of each time step, which are referred to the update-stress-first (USF) scheme and the update-stress-last (USL) scheme, respectively. In the modified update-stress-last (MUSL) scheme, the grid nodal velocity obtained by projecting the updated particle momentum back to the grid nodes is used to update the stress. The USL scheme is highly dissipative. Ni and Zhang⁶² proved that the USL scheme suffers from an extremely small critical time step when cell-crossing phenomenon occurs. Thus, the USF scheme is used in this work.

2.2 | Shortcomings of the standard MPM in shell simulations

The MPM suffers from several locking phenomena when modeling shell structures with a coarse background grid. For the sake of clarity, the pure bending deformation of a shell is studied. A coarse background grid whose cell size equals the shell thickness is adopted as shown in Figure 2A. In the thickness direction, only one layer of grid cells with trilinear shape function is involved in calculating the strain of particles. As one of the cells shown in Figure 2B, the initial configuration is represented by black dashed lines. The trilinear shape function of its node I is given as

$$N_I(\xi, \eta, \zeta) = \frac{1}{8} (1 + \xi_I \xi)(1 + \eta_I \eta)(1 + \zeta_I \zeta), \quad (17)$$

where (ξ, η, ζ) are the natural coordinates. A trilinear displacement field $\mathbf{u}(\mathbf{x})$ in the cell is obtained after substituting the shape function into Equation (3). With this displacement field, the deformed configuration of the cell in Figure 2B is different from the correct bending configuration (blue solid lines) in Figure 2C, which leads to shear locking, trapezoidal locking⁵⁶ and thickness locking¹ in the cell.

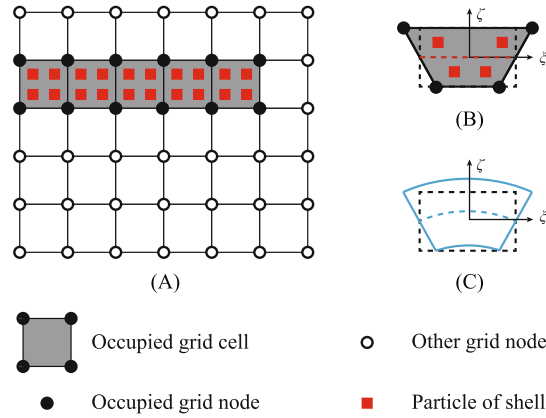


FIGURE 2 Bending process of MPM with a coarse background grid.

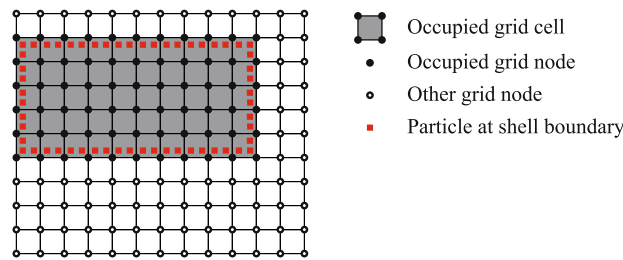


FIGURE 3 Discretized model of MPM with a fine background grid.

- (1) Shear locking appears with the spurious transverse shear strains at particles. The transverse shear strains of correct bending configuration are zero, while non-zero values at particles will be obtained by the trilinear shape function.
- (2) Trapezoidal locking^{56,57} occurs with the geometry of the cell becoming trapezoidal, which is inevitable. As shown in Figure 2B, the edge directors (the vectors from the lower node to the upper node of the edges) are not perpendicular to the mid-surface (red dashed line), which means the fibers along the thickness direction are stretched. That is, the trilinear shape function results in spurious transverse normal strain at particles.
- (3) Thickness locking¹ happens with the artificial normal stress in the thickness direction. For simplicity, the elastic constitutive model is considered, in which the stress $\sigma_{\zeta\zeta}$ is given as

$$\sigma_{\zeta\zeta} = \lambda(\varepsilon_{\xi\xi} + \varepsilon_{\eta\eta}) + (\lambda + 2\mu)\varepsilon_{\zeta\zeta}, \quad (18)$$

where λ and μ are Lamé constants, and $\varepsilon_{\zeta\zeta}$, $\varepsilon_{\xi\xi}$, and $\varepsilon_{\eta\eta}$ are the normal strains. In the pure bending configuration of the cell, $\varepsilon_{\zeta\zeta}$ is constant in the thickness direction, while $\varepsilon_{\xi\xi}$ and $\varepsilon_{\eta\eta}$ vary linearly in the thickness direction, so that a linear $\sigma_{\zeta\zeta}$ stress distribution is obtained. However, this artificial normal stress in the thickness direction contradicts the plane stress assumption, $\sigma_{\zeta\zeta} = 0$, in shell theory.

The locking phenomena lead to an overestimation of the strain and stress of particles and an underestimation of the deformation, which means an over stiff behavior of shell structures. In Section 6.2, this behavior is shown by the example of beam vibration. If the cell size of background grid is 1/2 of the shell thickness, the upper cells will be stretched and the lower cells will be compressed to describe bending deformation, which could alleviate the locking phenomena. However for the shell structure with large curvature in Section 6.4, the results of MPM are still wrong although taking the grid cell size as 1/2 of the shell thickness.

In order to eliminate the locking phenomena, the discretization size of background grid should be small enough, usually smaller than 1/5 of the shell thickness,⁵⁰ which however will lead to prohibitive computational cost. The discretized

model of the shell with a fine background grid is shown in Figure 3, where only the particles at the boundary are depicted for clarity. Compared with the coarse background grid in Figure 2, the length of each side of hexahedron cell is shortened to 1/5 and the number of grid cells increases by a factor of $5^3 = 125$. Besides, the time step is reduced to 1/5 with the critical time step in Equation (14). Hence, the computational cost becomes $5^4 = 625$ times that of the coarse background grid, which is undesirable and further illustrated in Section 6.2.

3 | SOLID SHELL MATERIAL POINT METHOD

In the present work, to simulate the deformation of shell structures with high computational efficiency, a novel solid shell material point method (SSMPM) is proposed by introducing the concept of shell particle and bending modes of solid shell element in material point method. In Section 3.1, the shell particle of SSMPM is presented. In order to describe the difference of strain field throughout the shell thickness, quadrature points are set on the shell particle domain. With the locking treatments in Section 3.2, a single layer of shell particles on a coarse background grid is able to correctly and efficiently simulate the deformation of shell structures.

3.1 | Shell particle

Figure 4 shows how the SSMPM represents the deformation of shell structures. In order to accurately describe the material domain in the framework of MPM, a single layer of shell particles with hexahedral particle domains is employed. The positions of the particle corners are also updated after integrating momentum equations on the background grid nodes to track the geometry of the particle domain. And in the present work, particle corners have only displacement DOFs which significantly facilitates the coupling with standard MPM particles. To calculate the correct strain field throughout the shell thickness, Gauss quadrature points (marked as “x” in Figure 4) are introduced into the shell particle. That means, the variation of strain field over the particle domain is considered, which is different from the CPDI2.³²

Based on the concept of the shell particle, after projecting the grid nodal displacement \mathbf{u}_I to particle corners with the shape function $N_I(\mathbf{x})$ of each grid node I , the displacement field $\mathbf{u}(\mathbf{x})$ of the computational domain is interpolated from the particle corner displacement \mathbf{u}_c by the shape function $S_c(\mathbf{x})$ of each particle corner c , namely

$$\mathbf{u}(\mathbf{x}) = \sum_{c=1}^{n_c} S_c(\mathbf{x}) \mathbf{u}_c, \quad (19)$$

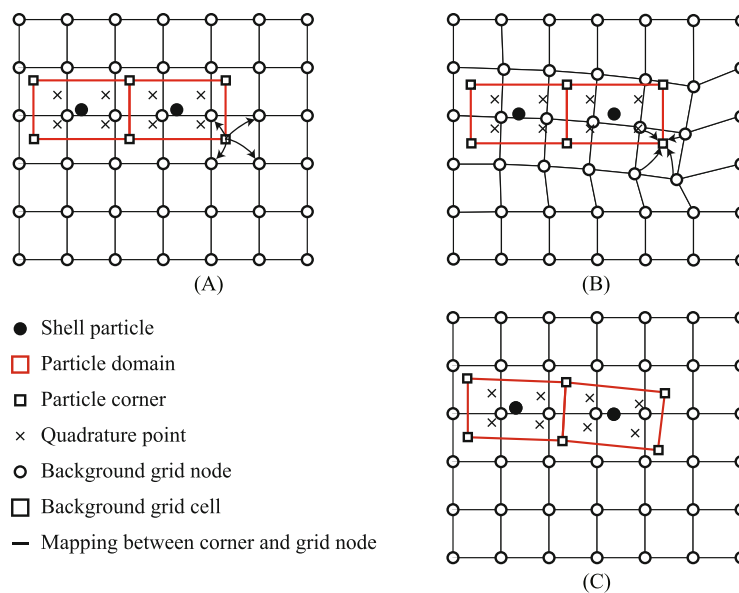


FIGURE 4 Computational process of the SSMPM.

$$\mathbf{u}_c = \sum_{I=1}^{n_g} N_{Ic} \mathbf{u}_I, \quad (20)$$

where the subscript c denotes the variables associated with particle corner c , n_c is the total number of particle corners, $S_c(\mathbf{x})$ is the trilinear shape function as that used in the FEM and $N_{Ic} = N_I(\mathbf{x}_c)$ is the shape function of the node I evaluated at the position of particle corner c .

Substituting Equations (19) and (20) into the weak form Equation (1) and invoking the arbitrariness of the virtual displacement $\delta \mathbf{u}_I$ lead to the same discretized momentum equations at each grid node as Equation (4). For the SSMPM, the lumped grid mass matrix is given by

$$m_I = \sum_{c=1}^{n_c} N_{Ic} m_c, \quad (21)$$

where

$$m_c = \sum_{p=1}^{n_p} \sum_{q=1}^{n_q} S_{cq}^p \rho V_q^p \quad (22)$$

is the mass of particle corner c . In Equation (22), $S_{cq}^p = S_c^p(\xi_q)$ is the shape function related to the c th corner of shell particle p evaluated at the q th quadrature point, V_q^p is the volume at the q th quadrature point of shell particle p and n_q is the number of quadrature points in a shell particle. The internal nodal force is

$$\mathbf{f}_I^{\text{int}} = \sum_{c=1}^{n_c} N_{Ic} \mathbf{f}_c^{\text{int}}, \quad (23)$$

where

$$\mathbf{f}_c^{\text{int}} = - \sum_{p=1}^{n_p} \sum_{q=1}^{n_q} \nabla S_{cq}^p \cdot \boldsymbol{\sigma}_q^p V_q^p \quad (24)$$

is the internal force of particle corner c , and $\boldsymbol{\sigma}_q^p$ is the stress at the q th quadrature point of shell particle p . The external nodal force is

$$\mathbf{f}_I^{\text{ext}} = \sum_{c=1}^{n_c} N_{Ic} \mathbf{f}_c^{\text{ext}}, \quad (25)$$

where

$$\mathbf{f}_c^{\text{ext}} = \sum_{p=1}^{n_p} \sum_{q=1}^{n_q} S_{cq}^p \rho \mathbf{b}_q^p V_q^p \quad (26)$$

is the external force of particle corner c with the traction term omitted for simplicity, and \mathbf{b}_q^p is the body force per unit mass of particle p at its q th quadrature point. Here, the strain rate and vorticity rate for calculating $\boldsymbol{\sigma}_q^p$ are given as

$$\dot{\boldsymbol{\epsilon}}_q^p = \frac{1}{2} (\mathbf{v}_c \otimes \nabla S_{cq}^p + \nabla S_{cq}^p \otimes \mathbf{v}_c), \quad (27)$$

$$\dot{\boldsymbol{\Omega}}_q^p = \frac{1}{2} (\mathbf{v}_c \otimes \nabla S_{cq}^p - \nabla S_{cq}^p \otimes \mathbf{v}_c), \quad (28)$$

where \mathbf{v}_c is the velocity of particle corner c , $\dot{\boldsymbol{\epsilon}}_q^p$ and $\dot{\boldsymbol{\Omega}}_q^p$ are the strain rate and vorticity rate at the q th quadrature point of shell particle p respectively.

For the computational process of SSMPM in Figure 4A, the grid nodal mass and forces are calculated by Equations (21)–(26), and the nodal momentum is given by

$$\mathbf{p}_I = \sum_{c=1}^{n_c} N_{Ic} m_c \mathbf{v}_c. \quad (29)$$

In Figure 4B, after updating the grid nodal acceleration \mathbf{a}_I^n at time t^n and velocity $\mathbf{v}_I^{n+1/2}$ at time $t^{n+1/2}$ by the same method as MPM, the velocities and positions of shell particle corners are updated by

$$\mathbf{v}_c^{n+1/2} = \mathbf{v}_c^{n-1/2} + \sum_{I=1}^{n_g} N_{Ic} \mathbf{a}_I^n \Delta t^n, \quad (30)$$

$$\mathbf{x}_c^{n+1} = \mathbf{x}_c^n + \sum_{I=1}^{n_g} N_{Ic} \mathbf{v}_I^{n+1/2} \Delta t^{n+1/2}, \quad (31)$$

so that the updated geometry of shell particles can be obtained in Figure 4C.

3.2 | Locking treatments

The shear locking, trapezoidal locking and thickness locking would cause an over stiff behavior of shell structures when using the shell particles in Section 3.1. The SSMPM avoids the locking effects by applying the assumed natural strain (ANS) method and enhanced assumed strain (EAS) method to the shell particles.

3.2.1 | Assumed natural strain (ANS) method

The assumed natural strain method^{54,55,57} is a successful tool to eliminate the shear locking and trapezoidal locking. The transverse normal strain $\varepsilon_{\zeta\zeta}$ and transverse shear strains $\varepsilon_{\eta\zeta}$, $\varepsilon_{\zeta\xi}$ at the quadrature points of shell particles are spurious due to the trilinear shape function of particle corners, which is detailed in Section 2.2. However, the above strain components can be correctly represented at suitable locations where required kinematic constraints for shell structures are satisfied.⁵⁷

In the natural coordinate system of the shell particle shown in Figure 5, the suitable locations called sampling points are located at the midpoints of the edges. Among these points, $\varepsilon_{\zeta\zeta}$ is correct at sampling points S_1, S_2, S_3, S_4 , $\varepsilon_{\eta\zeta}$, and $\varepsilon_{\zeta\xi}$ are respectively correct at sampling points S_5, S_6, S_7, S_8 , and $S_9, S_{10}, S_{11}, S_{12}$. In the ANS method, the respective strain components are evaluated at sampling points. Afterwards, the following interpolation schemes are conducted to calculate the values at quadrature points:

$$\varepsilon_{\zeta\zeta q}^p = \frac{1}{4} \sum_{I=S_1}^{S_4} (1 + \xi_I \xi_q) (1 + \eta_I \eta_q) \varepsilon_{\zeta\zeta I}^p, \quad (32)$$

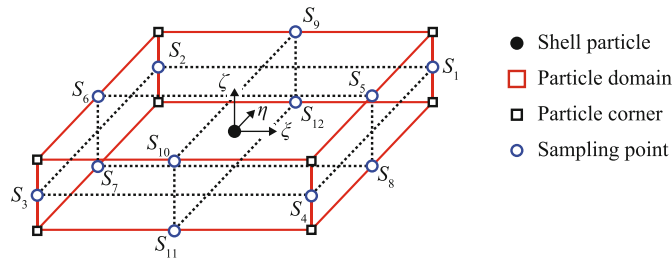


FIGURE 5 Diagram of the ANS method.

$$\varepsilon_{\eta\zeta q}^p = \frac{1}{4} \sum_{I=S_5}^{S_8} (1 + \xi_I \xi_q) (1 + \zeta_I \zeta_q) \varepsilon_{\eta\zeta I}^p, \quad (33)$$

$$\varepsilon_{\zeta\xi q}^p = \frac{1}{4} \sum_{I=S_9}^{S_{12}} (1 + \eta_I \eta_q) (1 + \zeta_I \zeta_q) \varepsilon_{\zeta\xi I}^p, \quad (34)$$

where $\varepsilon_{\zeta\xi q}^p$, $\varepsilon_{\eta\zeta q}^p$, and $\varepsilon_{\zeta\xi q}^p$ are the strain components at the quadrature point q of shell particle p , and $\varepsilon_{\zeta\xi I}^p$, $\varepsilon_{\eta\zeta I}^p$, and $\varepsilon_{\zeta\xi I}^p$ are the strain components at the sampling point I of shell particle p .

3.2.2 | Enhanced assumed strain (EAS) method

For the sake of clarity in this section, the variables with overbar or subscript ξ, η, ζ represent those in the natural coordinate system (ξ, η, ζ) and the others denote those in the global coordinate system (x, y, z) . For instance, the strains in the natural and global coordinate system are $\bar{\varepsilon}$ and ε respectively. The strain and stress are written in the vector form in this section, which means $\bar{\varepsilon} = [\varepsilon_{\xi\xi} \ \varepsilon_{\eta\eta} \ \varepsilon_{\zeta\zeta} \ \varepsilon_{\xi\eta} \ \varepsilon_{\eta\zeta} \ \varepsilon_{\zeta\xi}]^T$, $\varepsilon = [\varepsilon_{xx} \ \varepsilon_{yy} \ \varepsilon_{zz} \ \varepsilon_{xy} \ \varepsilon_{yz} \ \varepsilon_{zx}]^T$, and $\sigma = [\sigma_{xx} \ \sigma_{yy} \ \sigma_{zz} \ \sigma_{xy} \ \sigma_{yz} \ \sigma_{zx}]^T$.

As illustrated in Section 2.2, the thickness locking will occur in shell particles due to the trilinear shape function of particle corners. In order to prevent thickness locking, the enhanced assumed strain method^{58,59} is adopted in this work. Its core idea is to enhance the constant normal strain in the thickness direction by a linear extension. That is, in the natural coordinate system of the shell particle in Figure 5, the total strain field $\bar{\varepsilon}$ is split into the compatible strain field $\bar{\varepsilon}_c$ and enhanced assumed strain field $\bar{\varepsilon}_e$ as follows

$$\bar{\varepsilon} = \bar{\varepsilon}_c + \bar{\varepsilon}_e, \quad (35)$$

where $\bar{\varepsilon}_c = \bar{\mathbf{B}}_c \mathbf{u}$, $\bar{\mathbf{B}}_c$ is the strain operator, \mathbf{u} is the displacement of particle corners, and the enhanced assumed strain field is interpolated in the shell particle by

$$\bar{\varepsilon}_e = \bar{\mathbf{B}}_e \boldsymbol{\alpha}, \quad (36)$$

where $\bar{\mathbf{B}}_e$ is the enhanced assumed strain operator and $\boldsymbol{\alpha}$ is the enhanced degrees of freedom set at the particle centroid. To obtain a linear distribution of the normal strain in the thickness direction $\varepsilon_{\zeta\zeta}$, there are three options^{1,3,9,10} for $\bar{\mathbf{B}}_e$ and $\boldsymbol{\alpha}$

$$\bar{\mathbf{B}}_e = \begin{bmatrix} 0 \\ 0 \\ \zeta \\ 0 \\ 0 \\ 0 \end{bmatrix}, \begin{bmatrix} 0 & 0 & 0 \\ 0 & 0 & 0 \\ \zeta & \xi\zeta & \eta\zeta \\ 0 & 0 & 0 \\ 0 & 0 & 0 \\ 0 & 0 & 0 \end{bmatrix}, \text{ or } \begin{bmatrix} 0 & 0 & 0 & 0 \\ 0 & 0 & 0 & 0 \\ \zeta & \xi\zeta & \eta\zeta & \xi\eta\zeta \\ 0 & 0 & 0 & 0 \\ 0 & 0 & 0 & 0 \\ 0 & 0 & 0 & 0 \end{bmatrix}, \quad (37)$$

$$\boldsymbol{\alpha} = [\alpha_1], \begin{bmatrix} \alpha_1 \\ \alpha_2 \\ \alpha_3 \end{bmatrix}, \text{ or } \begin{bmatrix} \alpha_1 \\ \alpha_2 \\ \alpha_3 \\ \alpha_4 \end{bmatrix}. \quad (38)$$

The second type is adopted in the examples of Section 6. The thickness locking deficiency is then avoided by employing the enhanced assumed strain field $\bar{\varepsilon}_e$. In the global coordinate system, the compatible strain field ε_c and enhanced assumed strain field ε_e are given by

$$\varepsilon_c = \mathbf{T} \bar{\varepsilon}_c, \quad (39)$$

$$\varepsilon_e = \mathbf{T}_e \bar{\varepsilon}_e, \quad (40)$$

where \mathbf{T} is the transformation matrix as defined in Klinkel et al.⁵ and the transformation matrix \mathbf{T}_e will be given later.

With the definition of the enhanced assumed strain $\epsilon_e = \epsilon - \epsilon_c$, the approximate integral of the relation between strain and displacement

$$\int_{\Omega} \delta \boldsymbol{\sigma}^T (\boldsymbol{\epsilon} - \boldsymbol{\epsilon}_c) dV = 0 \quad (41)$$

becomes

$$\int_{\Omega} \delta \boldsymbol{\sigma}^T \boldsymbol{\epsilon}_e dV = 0 \quad (42)$$

which is called the orthogonality condition. In order to enforce Equation (42) to satisfy the patch test over each shell particle, the transformation matrix \mathbf{T}_e for the enhanced assumed strain field⁵⁸ is taken as

$$\mathbf{T}_e = \frac{|\mathbf{J}_0|}{|\mathbf{J}|} \mathbf{T}_0, \quad (43)$$

where \mathbf{J}_0 and \mathbf{T}_0 are the Jacobian matrix and transformation matrix at the particle centroid.

Substituting Equations (35), (39) and (40) into the weak form Equation (1), the second term of the weak form can be given as

$$\int_{\Omega} (\delta \boldsymbol{\epsilon}_c + \delta \boldsymbol{\epsilon}_e)^T \boldsymbol{\sigma} dV = 0, \quad (44)$$

where $\delta \boldsymbol{\epsilon}_e = \mathbf{B}_e \delta \boldsymbol{\alpha}$ and the enhanced degrees of freedom $\boldsymbol{\alpha}$ are the mean values in each particle. Then, invoking the arbitrariness of $\delta \boldsymbol{\alpha}$, a discretized equation over each shell particle is given as

$$\mathbf{f}_p^{\text{EAS}} = \mathbf{0}, \quad (45)$$

where

$$\mathbf{f}_p^{\text{EAS}} = \sum_{q=1}^{n_q} \mathbf{B}_{e,q}^T \boldsymbol{\sigma}_q^p V_q^p. \quad (46)$$

In each shell particle, Equation (45) can be solved by Newton iteration algorithm. In each iteration, the stress field is calculated by

$$\boldsymbol{\sigma}_{q,i}^{n+1} = \boldsymbol{\sigma}_q^n + \mathbf{D}_{ep,qi} \left(\Delta \boldsymbol{\epsilon}_{c,q}^n + \Delta \boldsymbol{\epsilon}_{e,qi}^n \right), \quad (47)$$

where $\mathbf{D}_{ep,qi}$ is the elastic–plastic constitutive matrix at the q th quadrature point and i is the number of iterations. For $\Delta \boldsymbol{\epsilon}_{c,q}^n$ in Equation (47), the modification applied to the compatible strain by ANS method, Equations (32)–(34), is included to eliminate shear locking and trapezoidal locking. Then Equation (46) is rewritten as

$$\mathbf{f}_{p,i}^{\text{EAS},n+1} = \sum_{q=1}^{n_q} \mathbf{B}_{e,q}^T \left[\boldsymbol{\sigma}_q^n + \mathbf{D}_{ep,qi} \left(\mathbf{B}_{c,q} \Delta \mathbf{u}^n + \mathbf{B}_{e,q} \Delta \boldsymbol{\alpha}_i^n \right) \right] V_q^p. \quad (48)$$

The tangent in Newton iteration algorithm is given as

$$\frac{\partial \mathbf{f}_{p,i}^{\text{EAS},n+1}}{\partial \Delta \boldsymbol{\alpha}_i^n} = \mathbf{K}_{e,i} = \sum_{q=1}^{n_q} \mathbf{B}_{e,q}^T \mathbf{D}_{ep,qi} \mathbf{B}_{e,q} V_q^p. \quad (49)$$

Therefore, the enhanced degrees of freedom at particle centroid can be updated by

$$\Delta \boldsymbol{\alpha}_{i+1}^n = \Delta \boldsymbol{\alpha}_i^n - \left(\frac{\partial \mathbf{f}_{p,i}^{\text{EAS},n+1}}{\partial \Delta \boldsymbol{\alpha}_i^n} \right)^{-1} \mathbf{f}_{p,i}^{\text{EAS},n+1}. \quad (50)$$

For elastic deformation, the tangent is independent of $\Delta\alpha_i^n$ so that only one iteration is needed. For plastic deformation, the convergence rate is fast because the deformation of particles is small in the small time steps of explicit algorithm. For instance, the example in Section 6.4 achieves accurate results with no more than five iterations.

4 | LOCAL MULTI-MESH CONTACT METHOD

Local multi-mesh contact method¹⁸ has been developed to couple two MPM bodies through the background grid. Furthermore, it was put forward to couple a FEM body and a MPM body in the coupled finite element material point (CFEMP) method.⁶⁰ From Section 3, it can be found that the SSMPM and MPM share the same nodal DOFs and they have a similar computational framework. Therefore, a local multi-mesh contact method is presented to naturally couple the SSMPM and MPM for the contact situations of shells with other objects. The contact method is also applicable to the contact situations of shell structures if the MPM body is replaced by SSMPM body, which will not be repeated.

The coupling of body r modeled by MPM and body s modeled by SSMPM is shown in Figure 6. In each time step, the velocities of two bodies at the same grid node can be obtained after independently updating body r and body s . And then, the contact state of each grid node is detected by its velocities of two bodies. Contact forces should be imposed between body r and body s to prevent penetration if contact occurs.

4.1 | Contact detection

The contact detection is based on the velocity fields of two bodies at background grid nodes. After calculating grid nodal mass and momentum by mapping those of MPM particles and SSMPM particle corners, the velocity of body b ($b = r, s$) at grid node I is given as

$$v_{il}^{b,n-1/2} = \frac{P_{il}^{b,n-1/2}}{m_I^{b,n}}. \quad (51)$$

Contact may take place at grid node I if its velocity is contributed by the two bodies. Furthermore, body r and body s will contact in the vicinity of grid node I if the following condition is satisfied

$$\left(v_{il}^{r,n-1/2} - v_{il}^{s,n-1/2}\right) n_{il}^{r,n} > 0, \quad (52)$$

where $n_{il}^{r,n}$ is the unit outward normal on the surface of body r at grid node I . $n_{il}^{r,n}$ of MPM body can be calculated by the gradient of the mass⁶³ as

$$n_{il}^{r,n} = \frac{1}{\left|\sum_{p=1}^{n_p} N_{Ip,i} m_p\right|} \sum_{p=1}^{n_p} N_{Ip,i} m_p \quad (53)$$

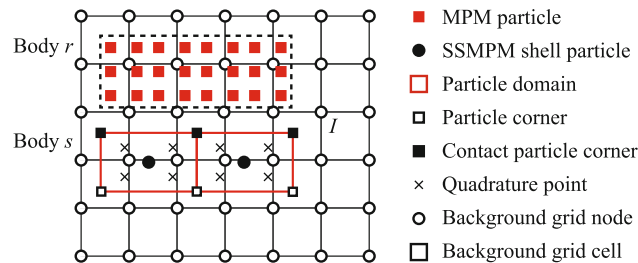


FIGURE 6 Diagram of coupling SSMPM with MPM.

or by $n_{ii}^{r,n} = -n_{ii}^{s,n}$, where $n_{ii}^{s,n}$ is the unit outward normal on the surface of SSMPM body at grid node I . With the surfaces of shell particles, $n_{ii}^{s,n}$ can be obtained by normalizing the normal vectors on the surfaces in which contact particle corners contributing to the grid node I are located.

Multiplied by $m_I^{r,n} m_I^{s,n}$, Equation (52) is rewritten in a momentum form as

$$\left(m_I^{s,n} p_{ii}^{r,n-1/2} - m_I^{r,n} p_{ii}^{s,n-1/2} \right) n_{ii}^{r,n} > 0. \quad (54)$$

Contact between two bodies will be detected earlier than actual contact time with Equation (54), so that the improved contact detection method¹⁸ is adopted here to avoid the earlier contact. The sizes of SSMPM particle domains should not exceed three grid cell sizes for proper contact detection.

4.2 | Contact force

Contact force $f_{ii}^{b,c,n}$ should be imposed on two bodies to prevent penetration if contact occurs at grid node I . After that, the momentum p_{ii}^b of body b ($b = r, s$) is updated by

$$p_{ii}^{b,n+1/2} = \bar{p}_{ii}^{b,n+1/2} + \Delta t^n f_{ii}^{b,c,n}, \quad (55)$$

where

$$\bar{p}_{ii}^{b,n+1/2} = p_{ii}^{b,n-1/2} + \Delta t^n f_{ii}^{b,n} \quad (56)$$

is the trial grid nodal momentum and $f_{ii}^{b,c,n}$ is the contact force applied on body b at time t^n . And the updated momentum should satisfy the impenetrability condition

$$\left(m_I^{s,n} p_{ii}^{r,n+1/2} - m_I^{r,n} p_{ii}^{s,n+1/2} \right) n_{ii}^{r,n} = 0. \quad (57)$$

The normal contact force $f_I^{\text{nor},n} = f_{ii}^{r,c,n} n_{ii}^{r,n} = -f_{ii}^{s,c,n} n_{ii}^{r,n}$ can be obtained by substituting Equation (55) into Equation (57) as

$$f_I^{\text{nor},n} = - \frac{\left(m_I^{s,n} \bar{p}_{ii}^{r,n+1/2} - m_I^{r,n} \bar{p}_{ii}^{s,n+1/2} \right) n_{ii}^{r,n}}{\left(m_I^{r,n} + m_I^{s,n} \right) \Delta t^n} = f_{I,1}^{\text{nor},n} + f_{I,2}^{\text{nor},n}, \quad (58)$$

where

$$f_{I,1}^{\text{nor},n} = - \frac{\left(m_I^{s,n} p_{ii}^{r,n-1/2} - m_I^{r,n} p_{ii}^{s,n-1/2} \right) n_{ii}^{r,n}}{\left(m_I^{r,n} + m_I^{s,n} \right) \Delta t^n}, \quad (59)$$

$$f_{I,2}^{\text{nor},n} = - \frac{\left(m_I^{s,n} f_{ii}^{r,n} - m_I^{r,n} f_{ii}^{s,n} \right) n_{ii}^{r,n}}{m_I^{r,n} + m_I^{s,n}}. \quad (60)$$

For stick contact, there is the non-slip condition

$$\left(m_I^{s,n} p_{ii}^{r,n+1/2} - m_I^{r,n} p_{ii}^{s,n+1/2} \right) t_{ii}^{r,n} = 0. \quad (61)$$

Substituting Equation (55) into Equation (61), the tangential contact force $f_I^{\text{stick},n} = f_{ii}^{r,c,n} t_{ii}^{r,n} = -f_{ii}^{s,c,n} t_{ii}^{r,n}$ is given as

$$\begin{aligned} f_I^{\text{stick},n} &= \frac{\left(m_I^{s,n} \bar{p}_{ii}^{r,n+1/2} - m_I^{r,n} \bar{p}_{ii}^{s,n+1/2} \right) t_{ii}^{r,n}}{\left(m_I^{r,n} + m_I^{s,n} \right) \Delta t^n} \\ &= \frac{\left(m_I^{s,n} p_{ii}^{r,n-1/2} - m_I^{r,n} p_{ii}^{s,n-1/2} \right) t_{ii}^{r,n}}{\left(m_I^{r,n} + m_I^{s,n} \right) \Delta t^n} + \frac{\left(m_I^{s,n} f_{ii}^{r,n} - m_I^{r,n} f_{ii}^{s,n} \right) t_{ii}^{r,n}}{m_I^{r,n} + m_I^{s,n}}, \end{aligned} \quad (62)$$

where

$$t_{ii}^{r,n} = \frac{\left(v_{ii}^{r,n-1/2} - v_{ii}^{s,n-1/2} \right) - \left(v_{ji}^{r,n-1/2} - v_{ji}^{s,n-1/2} \right) n_{ji}^{r,n} n_{ii}^{r,n}}{\left| \left(v_{ii}^{r,n-1/2} - v_{ii}^{s,n-1/2} \right) - \left(v_{ji}^{r,n-1/2} - v_{ji}^{s,n-1/2} \right) n_{ji}^{r,n} n_{ii}^{r,n} \right|} \quad (63)$$

is the unit tangent at grid node I .

For slip contact, the Coulomb friction model is employed. The friction force is limited to $\mu \|f_I^{\text{nor},n}\|$, where μ is the friction coefficient, namely

$$f_I^{\text{tan},n} = \min\left(\mu \|f_I^{\text{nor},n}\|, \|f_I^{\text{stick},n}\|\right). \quad (64)$$

Therefore, the contact force for body b is calculated by

$$f_{ii}^{b,c,n} = f_I^{\text{nor},n} n_{ii}^{b,n} + f_I^{\text{tan},n} t_{ii}^{b,n}. \quad (65)$$

The new regular background grid at the beginning of each time step is different from the deformed grid at the end of the previous time step. The impenetrability condition Equation (57) may not be satisfied at the beginning of each time step if it is applied at the end of the previous time step and the $f_{I,1}^{\text{nor},n}$ in Equation (59) is nonzero. Then, the nodal velocity $v_{ii}^{b,n-1/2}$ for updating the stress may disobey the impenetrability condition Equation (57), which would lead to disturbance to the system.¹⁷ In order to eliminate the artificial disturbance, after calculating grid nodal mass and momentum by mapping those of particles, $f_{I,1}^{\text{nor},n}$ is imposed to adjust the grid nodal momentum $p_{ii}^{r,n-1/2}$ to

$$\tilde{p}_{ii}^{r,n-1/2} = p_{ii}^{r,n-1/2} + \Delta t^n f_{I,1}^{\text{nor},n} n_{ii}^{r,n} \quad (66)$$

and the velocity of the contact particle corner in SSMPM body $v_{ic}^{s,n-1/2}$ to

$$\tilde{v}_{ic}^{s,n-1/2} = v_{ic}^{s,n-1/2} + \Delta t^n \sum_{I=1}^n f_{I,1}^{\text{nor},n} n_{ii}^{s,n} N_{Ic} / m_I^{s,n}. \quad (67)$$

5 | ALGORITHM SUMMARY

The overall computational process of SSMPM is summarized as follows:

1. Calculate grid nodal mass and momentum by mapping those at particle corners, Equations (21) and (29); Impose boundary conditions.
2. Detect contact state of each grid node. If Equation (54) is satisfied and the distance between two bodies is less than a specified value, the two bodies contact at the grid node I .
3. Adjust the momenta of contact grid nodes by Equation (66) and the velocities of contact particle corners by Equation (67).
4. Calculate the strain and vorticity increments on shell particles and modify the strain increment with the ANS and EAS methods by the Newton iteration algorithm as follows:
 - (a) Assign the initial values $i = 1$, and $\Delta \alpha_1^n = \Delta \alpha^{n-1}$;
 - (b) Calculate the strain increment by Equations (35), (39), and (40), update f_p^{EAS} by Equations (46) and (47).
 - (c) If $f_p^{\text{EAS}} > \text{Tol}$, update $\Delta \alpha_{i+1}^n$ by Equations (49) and (50), let $i = i + 1$ and go back to step (b). Otherwise, terminate the iteration.
5. Update the stress on shell particles by corresponding constitutive law. Calculate grid nodal force from particle corners by Equations (23)–(26).
6. For contact grid nodes, calculate the second term of the normal contact force by Equation (60) and the tangential contact force by Equation (64), and add the contact forces to nodal force.

7. Integrate grid nodal momentum equations.
8. Update the velocity and geometry of shell particles based on the grid nodal acceleration and velocity, Equations (30) and (31).

Remark: In the MPM, the strain of particles is calculated by the trilinear shape function of background grid. It would suffer from several locking phenomena when using a coarse grid for simulations of shell structures. And thus, a fine background grid is needed to present the correct strain field throughout the shell thickness. In the CPDI2, the deformation of material domain is exactly tracked by particle domains, so that the accuracy is relatively higher and numerical fracture is prevented. With the strain field assumed to be constant over each particle domain, adequate grid cells and particles through the thickness are also necessary to obtain the reasonable strain field. In the SSMPM, locking treatments of solid shell element are introduced into the shell particle. With the precise description of bending modes, a single layer of shell particles on a coarse background grid is enough for shell structures, which benefits the computational efficiency. The SSMPM will suffer from mesh distortion under extreme deformation due to the particle domains. The distortion can be avoided by modeling the parts with extreme deformation by MPM and other parts by SSMPM respectively. Furthermore, in the process from structural failure to fragments formation, the failed and distorted shell particles of SSMPM could be converted into the particles of standard MPM. The double interpolation process of particle domains and background grid brings smoothing effects in SSMPM. The error caused by the smoothing effects is negligible as shown by the results in the numerical examples in Section 6.

6 | NUMERICAL EXAMPLES

In this section, the convergence study of SSMPM is accomplished by the example of pinched cylinder with end diaphragms. The efficiency and capacity to circumvent locking phenomena are discussed by the vibration of a beam. And then, the ability of SSMPM to simulate the large deformation of shell structures is illustrated by the problems of pinched cylinder with free edges and full hemispherical shell. In addition, a contact situation of a shell structure with water is carried out by the water column collapse simulation. The penetration of a thin plate by a ball is simulated to demonstrate the advantage of SSMPM in extreme deformation and fragmentation of shell structures. Although the explicit SSMPM is proposed to simulate the dynamic problems, the quasi-static problems are studied in Sections 6.1, 6.3, and 6.4 by the dynamic relaxation process with artificial damping to verify the explicit SSMPM.

6.1 | Pinched cylinder with end diaphragms

Pinched cylinder with end diaphragms is a recognized benchmark example for shell structures in the literature. Alves et al.⁴ and Cardoso et al.⁶ used this example to assess the convergence behavior of the solid shell elements in FEM. As shown in Figure 7, the cylinder with length $L = 600\text{m}$, inner radius $R = 300\text{m}$ and thickness $t = 3\text{m}$ is constrained by two

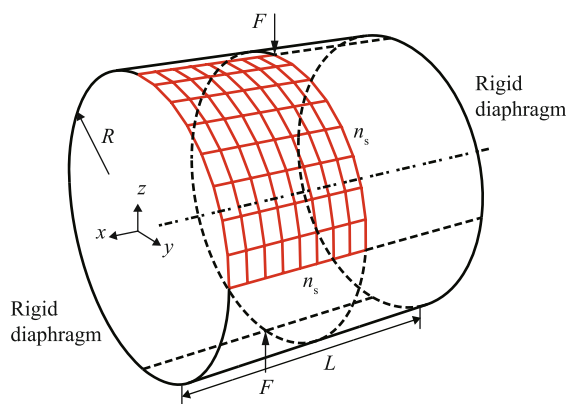


FIGURE 7 Diagram and discretization for pinched cylinder with end diaphragms.

rigid end diaphragms. And it has a density of $\rho = 3 \text{ kg/m}^3$, a Young's modulus of $E = 3 \text{ Pa}$ and a Poisson's ratio of $\nu = 0.3$. As a pair of diametrically opposite concentrated loads $F = 1 \text{ N}$ applied at the midpoints of the cylinder, the existence of both inextensional bending and complex membrane deformations leads to a severe test for SSMPM.

Due to symmetry, one-eighth of the cylinder in Figure 7 is discretized into $n_s \times n_s$ shell particles, where n_s denotes the number of shell particles per side. For the study of convergence, n_s is chosen as 4, 8, 12, 16, 20, 32, and 48, respectively. The background grid cell size is generally equal to the shell thickness to guarantee the spatial resolution in the thickness direction. And the results will not change much if the grid is further refined.

In order to validate the elimination of the three locking in SSMPM, the radial displacement at the loaded point is normalized by the reference solution of $1.82488 \times 10^{-5} \text{ m}$. And then, Figure 8A plots the curves of normalized displacement versus n_s obtained by five testing methods named as SSMPM, SSMPM ANS γ , SSMPM ANS $\gamma\epsilon$, SSMPM ANS γ -EAS, and SSMPM ANS $\gamma\epsilon$ -EAS. Figure 9 shows the configurations obtained by these schemes for $n_s = 48$, where the deformation is magnified 5×10^6 times for visibility. They have the same formulation of shell particle but different locking treatments:

- (1) SSMPM: without locking treatments, suffers from shear locking, trapezoidal locking and thickness locking;
- (2) SSMPM ANS γ : with the ANS method for shear locking, suffers from trapezoidal locking and thickness locking;
- (3) SSMPM ANS $\gamma\epsilon$: with the ANS method for shear locking and trapezoidal locking, suffers from thickness locking;
- (4) SSMPM ANS γ -EAS: with the ANS method for shear locking and the EAS method for thickness locking, suffers from trapezoidal locking;
- (5) SSMPM ANS $\gamma\epsilon$ -EAS: with the ANS method for shear locking and trapezoidal locking and the EAS method for thickness locking.

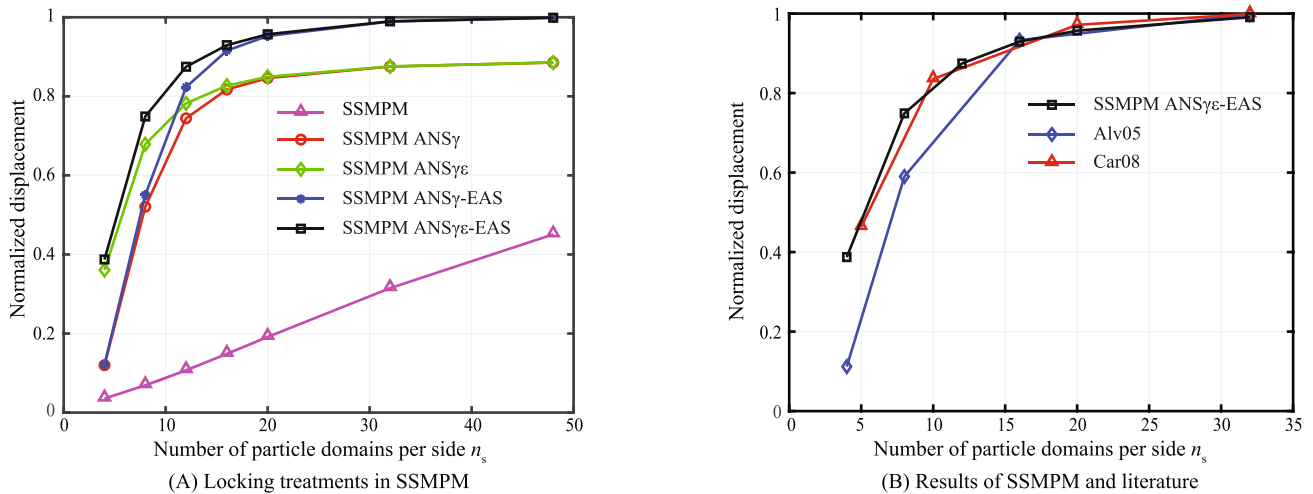


FIGURE 8 Plot of normalized displacement versus n_s .

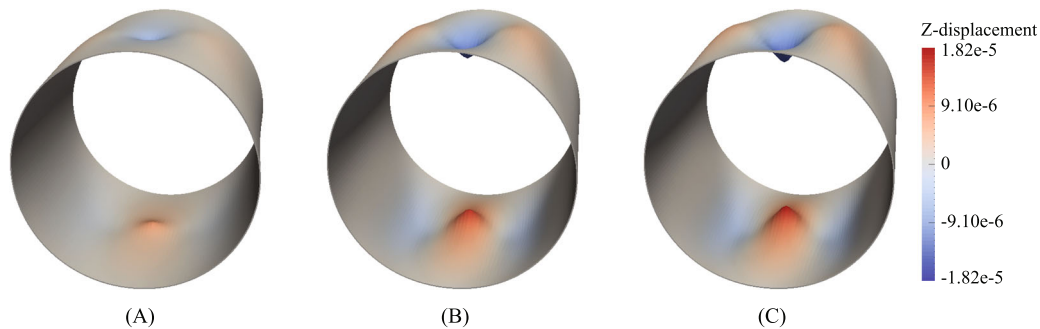


FIGURE 9 Configurations obtained with different methods for $n_s = 48$: (A) SSMPM, (B) SSMPM ANS $\gamma\epsilon$, (C) SSMPM ANS $\gamma\epsilon$ -EAS.

As shown in Figures 8A and 9A, the three locking mechanisms severely underestimate the displacement. In Figure 8A, with the ANS method for shear locking, the results of SSMPM ANS γ are significantly improved, which means shear locking has the greatest negative effect. However, the accuracy is pretty poor when few shell particles are employed and the displacement cannot converge to the reference solution when adequate shell particles are adopted. After introducing the ANS method for trapezoidal locking, SSMPM ANS $\gamma\epsilon$ performs better than SSMPM ANS γ when n_s is small. This is because shell particles are trapezoidal and trapezoidal locking exists when n_s is small. With adequate shell particles, the shape of particles is close to rectangle so that trapezoidal locking is not obvious and the results of SSMPM ANS $\gamma\epsilon$ are close to SSMPM ANS γ . And thus, the configuration of SSMPM ANS $\gamma\epsilon$ is shown in Figure 9B, which is obvious but the displacement is smaller than the reference solution. The EAS method helps the results of SSMPM ANS $\gamma\epsilon$ -EAS and SSMPM ANS $\gamma\epsilon$ -EAS in Figure 8A converge to the reference solution, which shows the necessity to eliminate thickness locking. The configuration of SSMPM ANS $\gamma\epsilon$ -EAS is shown in Figure 9C. Among the five testing methods, SSMPM ANS $\gamma\epsilon$ -EAS is free from the three locking and gives the best results.

In order to compare the convergence behavior of SSMPM ANS $\gamma\epsilon$ -EAS with the data in the literature, Figure 8B plots the curves obtained by SSMPM ANS $\gamma\epsilon$ -EAS, Alves et al.⁴ and Cardoso et al.⁶ When n_s is small, there are too few shell particles of SSMPM ANS $\gamma\epsilon$ -EAS and elements of FEM to accurately describe the cylinder, so that the results are poor in accuracy. As n_s increases, convergence to the reference solution is achieved by SSMPM ANS $\gamma\epsilon$ -EAS. In the first half of the curves shown in Figure 8, the results of SSMPM ANS $\gamma\epsilon$ -EAS and Cardoso et al.⁶ are more precise than those of Alves et al.,⁴ which indicates good convergence behavior of SSMPM ANS $\gamma\epsilon$ -EAS. For the sake of simplicity, the SSMPM ANS $\gamma\epsilon$ -EAS is abbreviated as SSMPM and employed in the rest part of this article.

6.2 | Beam vibration

In this section, the vibration of a cantilever beam⁵³ is simulated to verify the elimination of locking phenomena and the efficiency of SSMPM, compared to the standard MPM with different background grids. As shown in Figure 10, the beam has a length of $L = 100\text{m}$ and the square section with a width of $b = 1\text{m}$ and a thickness of $t = 1\text{m}$. The material parameters for the beam are density $\rho = 1\text{ kg/m}^3$, Young's modulus $E = 1.0 \times 10^8\text{Pa}$ and Poisson's ratio $\nu = 0.0$. A load $P = 10\text{N}$ applied at the center of the right end of the beam leads to the vibration.

In the case of static loading, the deflection at the center of the right end of the beam is $d_{\text{stat}} = FL^3/3EI = 4FL^3/Ebt^3 = 0.4\text{m}$. During the vibration, the maximum deflection is twice that in static loading, which is called dynamic amplification. The lowest natural frequency of the beam is $f = 1.875^2\sqrt{EI}/2\pi L^2\sqrt{\rho bt} = 0.16152\text{Hz}$, so that the period of the vibration is $T = 1/f = 6.191\text{s}$. As mentioned in Section 2.2, the maximum deflection and period of the beam will be underestimated if locking phenomena appear.

In SSMPM, the beam is discretized into n_s ($n_s = 5, 20, 50$) shell particles. Background grid cell size is 1m , which means the number of grid cells through the beam thickness $n_t = 1$. Figure 11 depicts the time history of the deflection at the right upper corner of the beam obtained by SSMPM. And the result of the ABAQUS with 50 S4R elements is adopted as a reference solution. When $n_s = 5$, a minor error between the SSMPM and reference solution is caused by the sparse discretization, while the SSMPM predicts the consistent results compared with the reference solution when $n_s = 20, 50$. As listed in Table 1, the maximum deflection and period in the results of SSMPM and reference solution are in good agreement with the theoretical values, which illustrates that locking effects are eliminated.

To investigate the locking effects in MPM and GIMP, four discretized models with $n_t = 1, 2, 4, 5$ are employed. Namely, the particle spaces are $d_p = 0.5, 0.25, 0.125, 0.1\text{m}$ and grid cell sizes are $d_g = 1, 0.5, 0.25, 0.2\text{m}$. Figure 12 compares the time history curves obtained by MPM, GIMP and the reference solution. Table 1 shows the maximum deflection and period of MPM. For GIMP ($n_t = 1$), the maximum deflection and period of are 0.15 m and 2.38 s , respectively. The values of GIMP

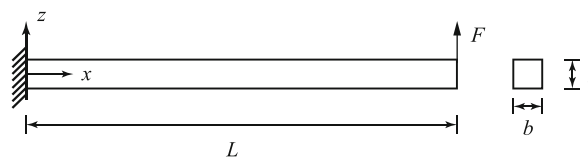


FIGURE 10 Diagram for cantilever beam.

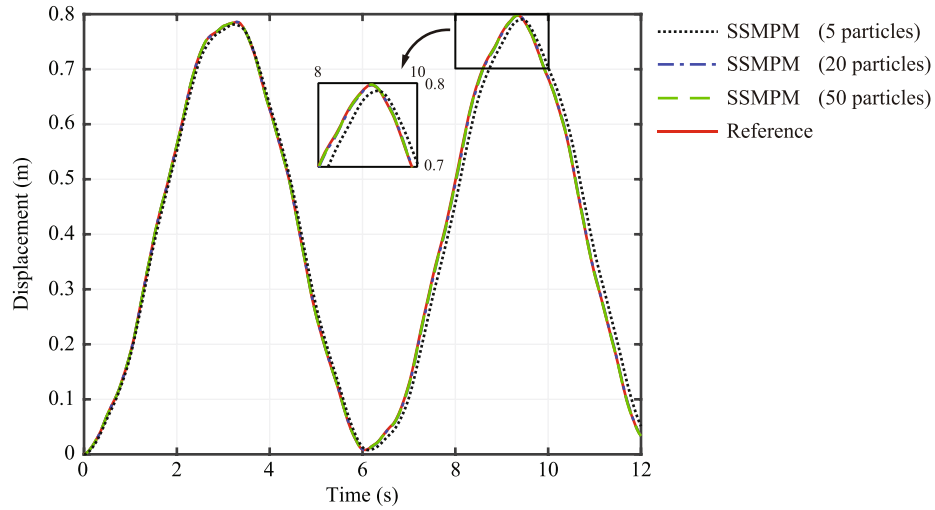


FIGURE 11 Time histories of the deflection at the right upper corner of the beam obtained by SSMPM and ABAQUS.

TABLE 1 Maximum deflection, period of vibration and CPU time of different methods.

	Theoretical	ABAQUS	SSMPM ($n_t = 1$)			MPM			
			$n_s = 5$	$n_s = 20$	$n_s = 50$	$n_t = 1$	$n_t = 2$	$n_t = 4$	$n_t = 5$
Maximum deflection (m)	0.80	0.80	0.79	0.80	0.80	0.42	0.77	0.79	0.79
Period of vibration (s)	6.19	6.06	6.12	6.06	6.06	4.19	5.95	6.02	6.03
CPU time (s)	-	-	43	77	191	51	812	15161	36816

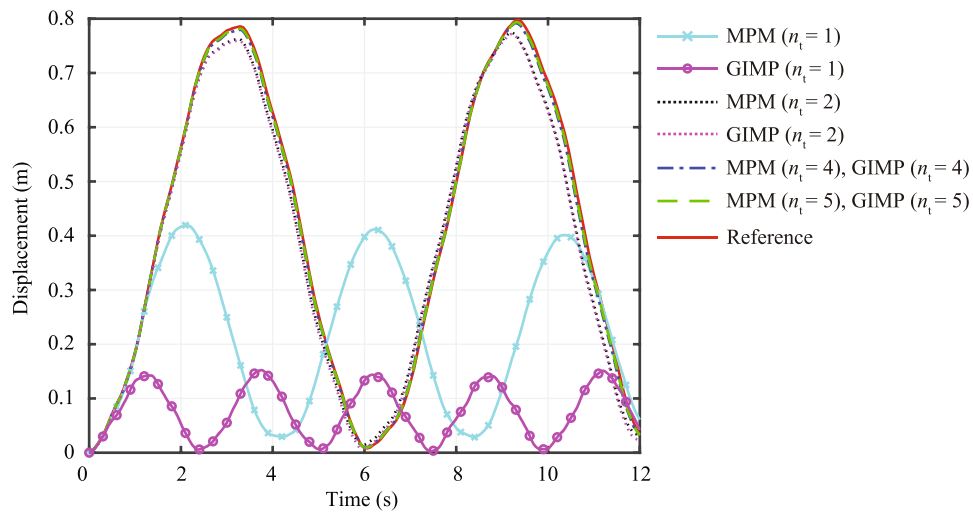


FIGURE 12 Time histories of the deflection at the right upper corner of the beam obtained by MPM and ABAQUS.

($n_t = 2, 4, 5$) are same as those of MPM ($n_t = 2, 4, 5$). When $n_t = 1$, the results of MPM and GIMP are obviously smaller than the reference solution, which is resulted from the severe locking phenomena. For $n_t = 2$, bending deformation is described by a layer of stretched cells and a layer of compressed cells, and there are three layers of grid cells through the beam thickness due to the cell-crossing of particles. Therefore, the error from locking effects becomes small. With $n_t = 4$ and 5, background grid is fine enough to overcome the shortcomings of locking and the results are consistent with the reference solution.

To study the efficiency of SSMPM compared to MPM and GIMP, Table 1 summarizes the CPU time of different discretized models in SSMPM and MPM. For GIMP ($n_t = 1, 2, 4, 5$), CPU times are 180, 2788, 45,728, and 112,721 s respectively. For $n_t = 1$, SSMPM costs a similar amount of CPU time as MPM, which indicates that the algorithm complexity of SSMPM is close to that of MPM. With n_t of MPM increasing, the number of background grid cells increases by n_t^3 times and the time step reduces by $1/n_t$, so that the total computational cost of MPM is proportional to n_t^4 . The computational cost of MPM ($n_t = 2$) and MPM ($n_t \geq 4$) respectively reaches over 10 and 100 times those of MPM ($n_t = 1$) and SSMPM. This law also applies to GIMP and GIMP costs more than MPM due to the shape function with larger support domain.

As a summary, in the vibration of this cantilever beam, locking effects result in the poor accuracy of the MPM with a coarse background grid. As the grid refined, the shortcomings of MPM are overcome, however its computational cost increases rapidly. In contrast, without locking phenomena, the SSMPM can precisely and effectively simulate bending deformation.

6.3 | Pinched cylinder with free edges

Pinched cylinder with free edges⁷ is a classical case for testing the ability to simulate large bending and membrane deformations and to capture buckling phenomena. As shown in Figure 13, the cylinder with a length of $L = 10.35$ mm, a radius of $R = 4.953$ mm and a thickness of $t = 0.094$ mm is unconstrained. The material has a density of $\rho = 7.8 \times 10^{-9}$ g/mm³, a Young's modulus of $E = 10.5 \times 10^6$ MPa and a Poisson's ratio of $\nu = 0.3125$. A pair of diametrically opposite concentrated loads F are applied at the midpoints of the cylinder.

In SSMPM, one eighth of the cylinder is discretized into 16×24 shell particles (16 shell particles in the axial direction, 24 shell particles in the tangential direction and 1 shell particle in the thickness direction) as shown in Figure 13. And the background grid cell size is 0.08 mm. For $F = 40$ kN, Figure 14 shows the dynamic relaxation process of SSMPM from initial state ($t = 0$) to equilibrium state ($t = t_e$), in which the loads increase linearly from zero to maximum and artificial damping is adopted to suppress oscillation. In the process from Figure 14A–C, the cylinder deformation is dominated by bending. The buckling phenomenon takes place at Figure 14C and the subsequent deformation from Figure 14C,D is mainly membrane stretching.

The radial displacements at points A, B, and C as shown in Figure 13 can be obtained after the cylinder is dynamic relaxed to the equilibrium state. Figure 15 plots the curves of loads F versus the displacements at corresponding equilibrium state obtained by SSMPM. And the results from published literature⁷ (represented as Sch10) and the FEM with

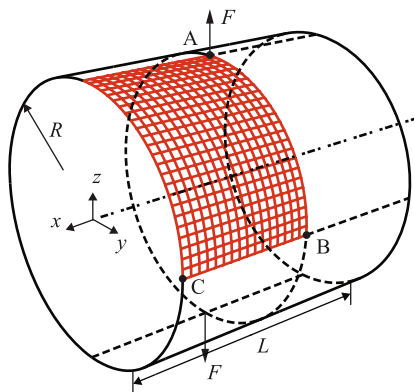


FIGURE 13 Diagram and discretization for pinched cylinder with free edges.

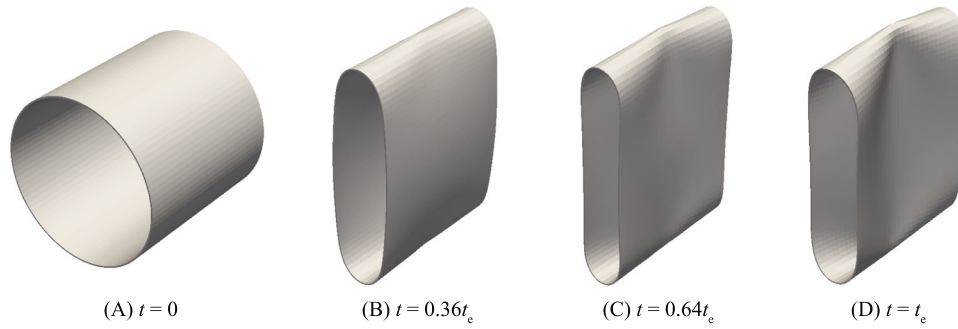


FIGURE 14 Dynamic relaxation process under $F = 40$ kN obtained by SSMPM.

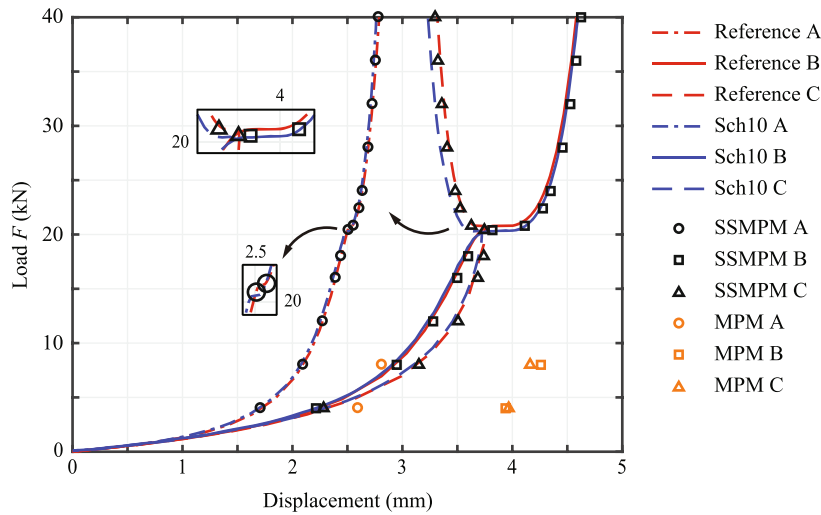


FIGURE 15 Plot of load F versus displacements of the points A, B, and C.

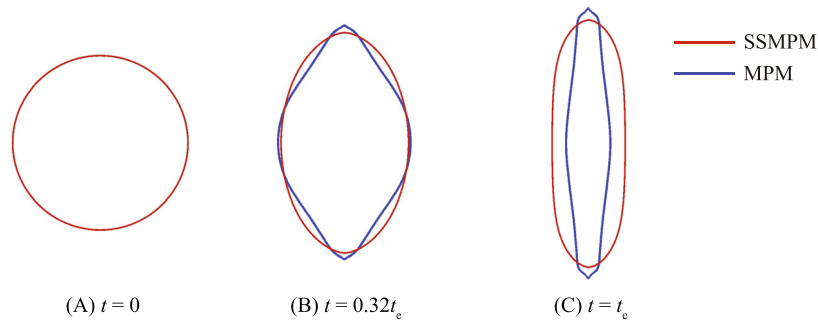


FIGURE 16 The middle cross sections in the dynamic relaxation process of SSMPM and MPM.

64 × 64 CSS8 elements in ABAQUS (denoted as Reference) are also given for comparison. When $F < 20$ kN, the loads are not enough for the buckling of the cylinder and the radial displacements at the points increase as the F increases. Characterized by the abrupt changes of the displacements, buckling takes place with the F reaching a critical value which is about 20 kN. There are small changes of the displacements for the membrane deformation when $F > 20$ kN. SSMPM is in good agreement with the reference data in the buckling critical value of loads and the displacements at different load cases, which verifies the ability of SSMPM to simulate large bending and membrane deformations and buckling phenomena of shell structures.

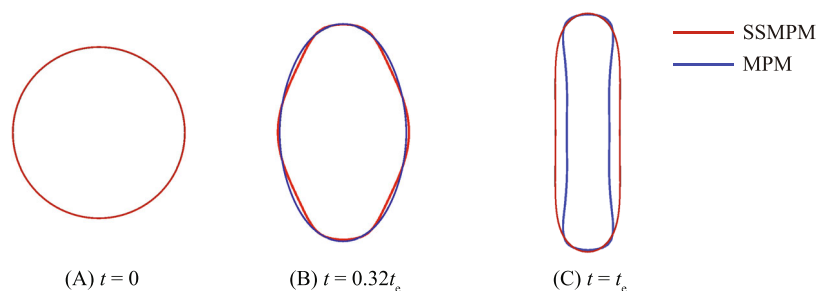


FIGURE 17 The cross sections at point C in the dynamic relaxation process of SSMPM and MPM.

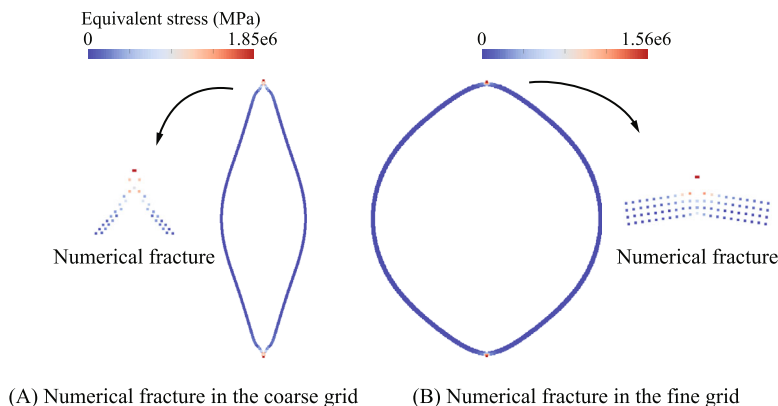


FIGURE 18 Numerical fracture of MPM.

Figure 15 also plots the results from the MPM with one layer of grid cells through the cylinder thickness, namely $n_t = 1$, the particle space $d_p = 0.047$ mm and grid cell size $d_g = 0.094$ mm. At the same loads, the displacements obtained by MPM are far greater than the reference data. Taking $F = 8$ kN for example, the middle cross sections in the dynamic relaxation process of SSMPM and MPM are compared in Figure 16 and the cross sections at point C of them are also illustrated in Figure 17. With the loads smaller than the buckling critical value, the cylinder is mainly subjected to bending deformation. As shown in Figures 16 and 17, SSMPM (red lines) gives the correct bending deformation. However in the results of MPM (blue lines), little bending deformation occurs at the upper and lower ends due to the locking phenomena. And thus, the rest of the cylinder is straightened under the pinched loads. When $F > 8$ kN, shear locking will lead to excessive local shear deformation at load points. And concentrated loads will directly cause the excessive local deformation in the fine background grid ($n_t \geq 2$). In these cases, numerical fracture will take place as shown in Figure 18, so that no results can be obtained.

For MPM ($n_t = 1$) and SSMPM, CPU times are 5990 and 6125 s, respectively. The computational cost of MPM ($n_t = 4$) can be speculated by the law given at the end of Section 6.2, which could reach over 100 times those of MPM ($n_t = 1$) and SSMPM.

In conclusion, for this cylindrical shell, shear locking results in the poor accuracy of the MPM with a coarse background grid. If employing a fine background grid, the MPM would suffer from numerical fracture, and its computational cost would be prohibitively high. For the SSMPM, large bending and membrane deformations and buckling phenomena can be accurately simulated with high efficiency.

6.4 | Full hemispherical shell

Full hemispherical shell⁵ is a test to the capacity for inextensible bending and rigid body modes. The shell with radius $R = 10.0$ mm and thickness $t = 0.5$ mm is unconstrained as shown in Figure 19. The strength model of the shell is described by

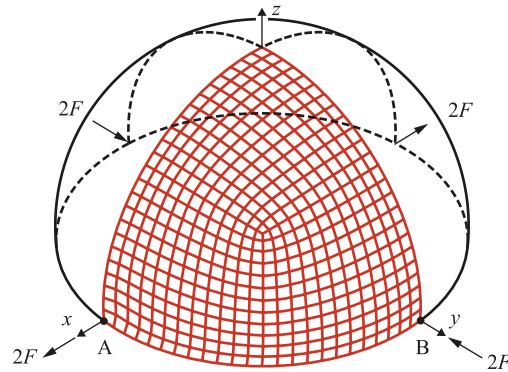


FIGURE 19 Diagram and discretization for the full hemispherical shell.

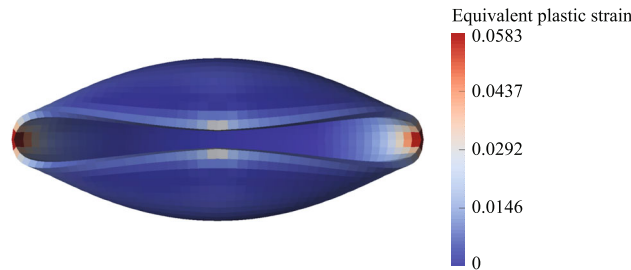


FIGURE 20 Deformed configuration at $F = 0.04$ kN in SSMPM.

elasto–plastic constitutive law with linear isotropic hardening. The material parameters are density $\rho = 1 \times 10^{-9}$ g/mm³, Young's modulus $E = 10$ MPa, Poisson's ratio $\nu = 0.2$, initial yield stress $\sigma_{y0} = 0.2$ MPa and plastic hardening modulus $H_{iso} = 9$ MPa. Four central symmetry concentrated loads are applied to the shell.

In SSMPM, owing to symmetry, one quarter of the shell is divided into three parts and each part is discretized into 12×12 shell particles as shown in Figure 19. And the background grid cell size is 0.4 mm. For $F = 0.04$ kN, the deformation of the shell obtained by dynamic relaxation is shown in Figure 20, in which the equivalent plastic strain is also depicted. The maximum of the equivalent plastic strain 5.83% appears at point A. And contact would occur at point B if larger loads are adopted.

With the two surfaces of shell structures given explicitly, the radial displacements at the inner and outer points of A and B shown in Figure 19 can be obtained after the shell is dynamically relaxed to the equilibrium state. As shown in Figure 21, the curves of loads F versus the displacements obtained by SSMPM are depicted. The data from published literature⁵ (denoted as Kli06) and the FEM with the CSS8 element in ABAQUS (represented as Reference) are also given for comparison. The consistent curves of the displacements at different load cases demonstrate the good agreement of SSMPM with these reference data, which verifies the capacity of SSMPM for simulating inextensible bending and rigid body modes of shell structures.

In MPM, two discretized models with one and two layers of grid cells through the cylinder thickness are employed. Namely, $n_t = 1, 2$, particle spaces are $d_p = 0.25, 0.125$ mm and grid cell sizes are $d_g = 0.5, 0.25$ mm. As shown in Figure 21, the results of MPM are larger than the reference data. For clarity, the cross sections at point B obtained by SSMPM and MPM with $F = 0.025$ kN are illustrated in Figure 22, where the configuration of SSMPM is reasonable, while that of MPM shows an over soft behavior. That is because the MPM with a coarse grid lacks of the capacity for inextensible bending, and then excessive rigid body displacement appears to resist loads.

As the results of MPM ($n_t = 1$) shown in Figures 21 and 22, the premature occurrence of the contact at point B when $F = 0.025$ kN causes the stop of deformation even though the loads increase, so that the results when $F > 0.025$ kN are same as those of $F = 0.025$ kN and not shown in Figure 21. For MPM ($n_t = 2$) and $F > 0.01$ kN, numerical fracture at point B will take place due to the concentrated loads as shown in Figure 23. And then, no data can be obtained.

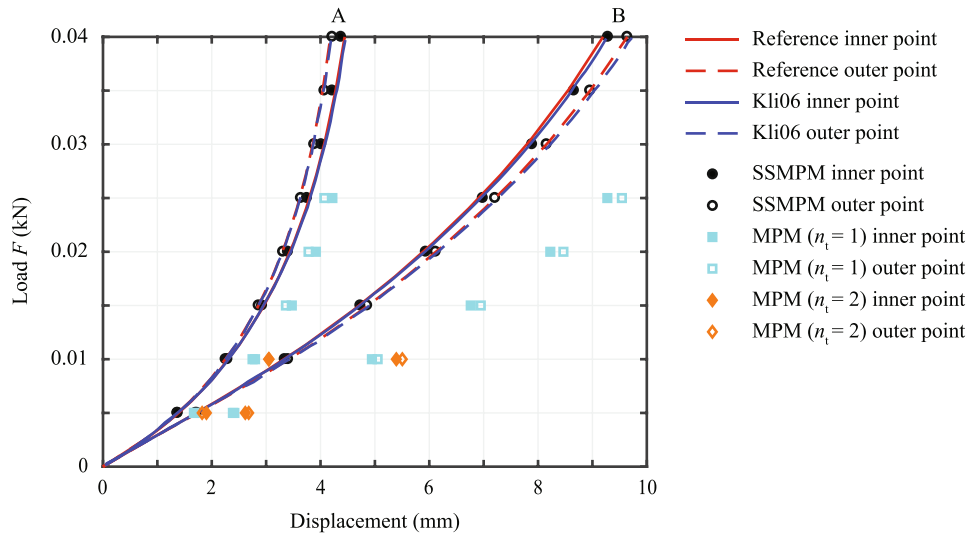


FIGURE 21 Plot of load F versus displacements at the inner points and outer points of A, B.

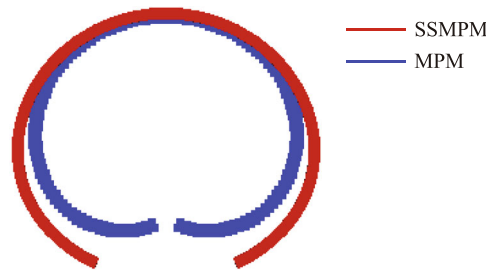


FIGURE 22 The cross sections at point B obtained by SSMPM and MPM.

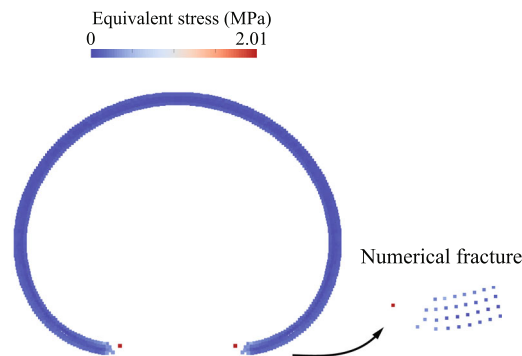


FIGURE 23 Numerical fracture of MPM.

For MPM ($n_t = 2$) and SSMPM, CPU times are 1788 and 1185s, respectively. The computational cost of MPM ($n_t = 4$) can be speculated by the law given at the end of Section 6.2, which could reach over 20 times that of SSMPM.

This example shows that correct bending deformation of the spherical shell could not be produced by MPM with a coarse background grid. Adopting the fine background grid in MPM would lead to numerical fracture and high computational cost. To overcome the shortcomings, the SSMPM is recommended to efficiently simulate deformation of shell structures.

6.5 | Water column collapse simulation

The large deformation of a shell in the fluid–structure interaction problem is investigated by SSMPM, MPM and their contact method. As shown in Figure 24, a water column will collapse through an elastic shell to the right wall due to the gravity. The shell has a thickness of $t = 12$ mm and a height of 80 mm, and the water column has a width of $L = 146$ mm and a height of $2L$. The distance from shell to water column is L .

The material parameters of the shell are density $\rho = 2.5\text{g/mm}^3$, Young's modulus $E = 1$ MPa and Poisson's ratio $\nu = 0$. The water column is described by Mie–Gruneisen EOS, whose material parameters are $\rho = 1000$ kg/m³, $c_0 = 1647$ m/s, $s = 1.921$, and $\gamma_0 = 0.1$. The water column will collapse freely due to the downward gravity with $g = 9.8$ mm/ms². The air and the friction between water column and shell are neglected. The shell is simulated by 16 shell particles in SSMPM. The water column is simulated by MPM in which particle space is 2 mm. The background grid size is 6 mm and the contact distance is set to 1 mm. In order to keep the surface of water smoothed, the water is assumed to be able to sustain maximum tension of 0.006 MPa. Plane strain is also assumed in the simulation.

As shown in Figure 25, both the deformation of the shell and the profile of the free surface obtained by SSMPM agree well with those obtained by ICFEMP,⁶⁴ CFEMP,⁶⁰ and PFEM.⁶⁵ The time history of the deflection at the left upper corner

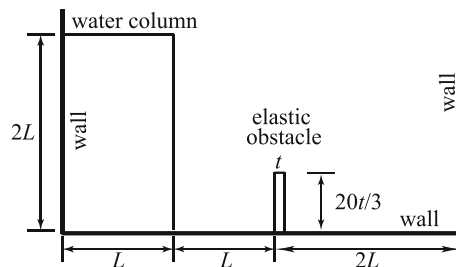


FIGURE 24 Diagram for the water column and elastic shell.

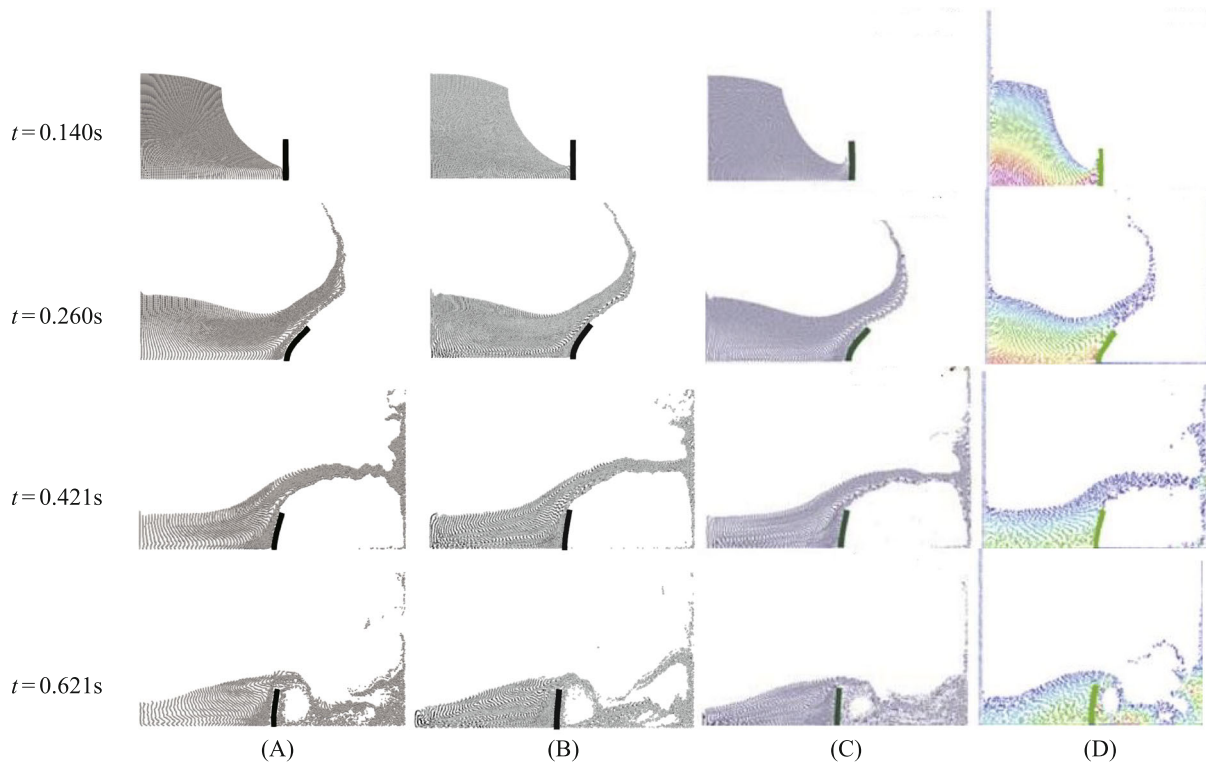


FIGURE 25 Numerical results at different times: (A) SSMPM, (B) ICFEMP, (C) CFEMP, (D) PFEM.

of the shell obtained by SSMPM also agrees well with other results^{60,64-66} in Figure 26. Among the different methods, SSMPM, CFEMP and ICFEMP all use MPM to simulate the water. The CPU time of SSMPM, CFEMP and ICFEMP are 83, 128 and 552 min, respectively. The SSMPM uses a coarse background grid and becomes more efficient than CFEMP. The ICFEMP is the least efficient due to the complex particle-to-surface contact method.

6.6 | Penetration of a thin plate by a ball

In order to demonstrate the advantage of SSMPM in extreme deformation and fragmentation of shell structures, the penetration of a thin circular plate with a thickness of 1 mm and a diameter of 178 mm by a ball with a diameter of 10 mm is investigated. The speed of the ball is 200 m/s and the direction of impact is normal to the thin plate.

The material of the ball and plate is steel and is described by elasto–plastic constitutive law with isotropic hardening

$$\sigma_y = A + B\bar{\epsilon}_p^n, \quad (68)$$

where A , B , and n are the material constants, σ_y is the flow stress and $\bar{\epsilon}_p$ is the effective plastic strain. The material constants of the steel are taken from the experiment⁶⁷ and listed in Table 2. According to De Vuyst et al.,⁶⁸ the failure of a MPM particle can be taken into account by setting the deviatoric components of the stress tensor to zero when the effective plastic strain reaches the failure strain. The failure strain $\bar{\epsilon}_{fail}$ for steel is set equal to 0.57.

The treatment of particle failure allows MPM to easily simulate the penetration of the plate. The SSMPM can accurately and effectively simulate the bending of the plate and is naturally coupled with MPM by the background grid. Therefore, the failure part of the plate is simulated by MPM and other parts are simulated by SSMPM. As shown in Figure 27, one quarter of the plate is discretized into 7296 shell particles of SSMPM (red) and 1008 particles of MPM (blue). The inner and outer diameters of the MPM region are 2.75 and 5.25 mm, respectively. And the ball is discretized into 8388 particles.

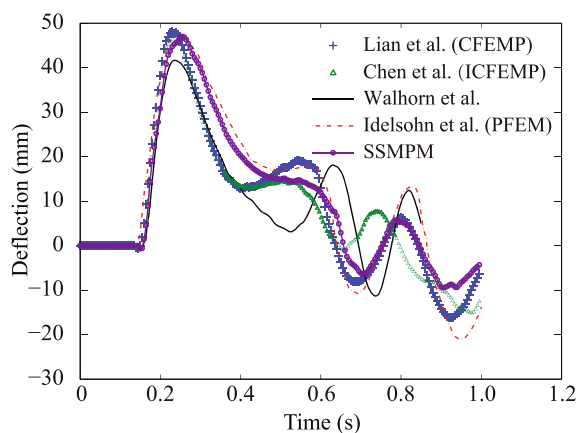


FIGURE 26 Time history of the deflection at the upper left corner of the shell obtained by different methods.

TABLE 2 Material constants of steel.

ρ (kg/m ³)	E (GPa)	ν	A (MPa)	B (MPa)	n	$\bar{\epsilon}_{fail}$
7850	200.0	0.30	600.0	275.0	0.36	0.57



FIGURE 27 Diagram for the plate and ball.

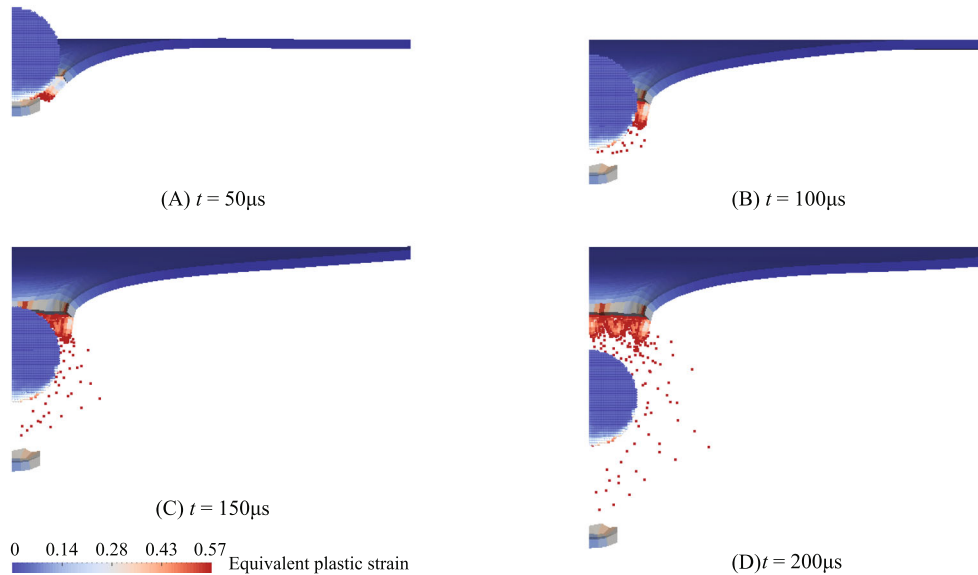


FIGURE 28 The configurations at various time step.

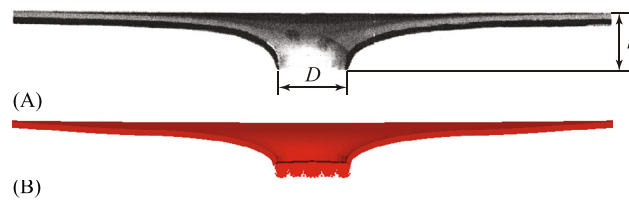


FIGURE 29 Final deformed shape of the thin plate: (A) experimental graph; (B) obtained by simulation.

The background grid size is 0.5 mm to alleviate the locking effects of the MPM part. The friction is neglected and the contact distance is set to 0.25 mm.

As shown in Figure 28, some MPM particles of the plate fail, allowing the plate to be perforated by the ball. None of SSMPM shell particles fail because the maximum effective plastic strain is equal to 0.54. The ball's residual velocities obtained from simulation is 79.0 m/s. Figure 29 compares the final deformed thin plate obtained from the experiment⁶⁷ and simulation. In Figure 29, h is the height of the final deformed plate and D is the diameter of penetrated hole. The value of h/D obtained in the experiment is 0.84, and that obtained from simulation is 0.87. The final deformed target plate obtained by simulation appears to be consistent with the experimental result.

In this example, the location of the fragmentation is known in advance and discretized by MPM particles. The number of grid cells through the thickness of MPM particles is 2. The MPM part still suffer from locking effects to a certain extent. However, the advantage of MPM in simulating the fragmentation of the plate is critical.

7 | CONCLUSION

In this article, a solid shell material point method (SSMPM) is proposed to efficiently model the large deformation of thin structures. The SSMPM describes the material domain of shell structures by shell particles with hexahedral particle domains. The locking treatments of solid shell element are then introduced in SSMPM, which results in the correction of strain field throughout the shell thickness. Namely, with the ANS method to eliminate shear locking and trapezoidal locking and the EAS method to eliminate thickness locking, a single layer of shell particles in the thickness direction is enough to simulate shell structures. With the precise description of bending modes, a coarse background grid could be used in SSMPM, which benefits the computational efficiency. With the same nodal DOFs of SSMPM and MPM, a local multi-mesh contact method is presented to naturally couple them for the contact situations of shells with other objects.

We carry out a benchmark example of pinched cylinder with end diaphragms to verify the convergence behavior of SSMPM. The case of beam vibration is conducted to validate SSMPM. The curves of SSMPM are consistent with the reference solution by FEM, which validates the elimination of locking effects. And SSMPM has a much smaller CPU time cost than the MPM with correct results, which illustrates the high efficiency. In addition, SSMPM and MPM are used to simulate the cases of pinched cylinder with free edges and full hemispherical shell. All the results of SSMPM are in great agreement with the data in the literature and reference solution by FEM, which shows the advantage of SSMPM over MPM in the shell structure simulations. Finally, with local multi-mesh contact method we apply SSMPM and MPM to investigate the water column collapse simulation, in which SSMPM correctly simulate the large deformation of a shell in the fluid–structure interaction problem.

In the simulation of penetration of a thin plate by a ball, the advantages of the MPM to simulate fragmentation and the SSMPM to simulate bending deformation are combined. Furthermore, shell structures could be discretized by shell particles only, and failed shell particles could be automatically converted into MPM particles. Therefore, the bending deformation of whole shell structures could be accurately simulated by SSMPM, and MPM particles automatically appear at fractures. The conversion scheme will be implemented in future work.

FUNDING INFORMATION

This work was supported by the National Natural Science Foundation of China with Grant Number 12172192.

DATA AVAILABILITY STATEMENT

The data that support the findings of this study are available from the corresponding author upon reasonable request.

ORCID

Xiong Zhang  <https://orcid.org/0000-0001-9905-281X>

REFERENCES

- Hauptmann R, Schweizerhof K. A systematic development of ‘solid-shell’ element formulations for linear and non-linear analyses employing only displacement degrees of freedom. *Int J Numer Methods Eng*. 1998;42(1):49-69.
- Sze K, Zheng SJ. A stabilized hybrid-stress solid element for geometrically nonlinear homogeneous and laminated shell analyses. *Comput Methods Appl Mech Eng*. 2002;191(17):1945-1966.
- Vu-Quoc L, Tan X. Optimal solid shells for non-linear analyses of multilayer composites. I. Statics. *Comput Methods Appl Mech Eng*. 2003;192(9):975-1016.
- dRJ SA, Cardoso RP, Fontes Valente RA, Yoon JW, Gracio JJ, Natal Jorge RM. A new one-point quadrature enhanced assumed strain (EAS) solid-shell element with multiple integration points along thickness: Part I – geometrically linear applications. *Int J Numer Methods Eng*. 2005;62(7):952-977.
- Klinkel S, Gruttmann F, Wagner W. A robust non-linear solid shell element based on a mixed variational formulation. *Comput Methods Appl Mech Eng*. 2006;195(1):179-201.
- Cardoso RPR, Yoon JW, Mahardika M, Choudhry S, Alves de Sousa A, Fontes Valente RA. Enhanced assumed strain (EAS) and assumed natural strain (ANS) methods for one-point quadrature solid-shell elements. *Int J Numer Methods Eng*. 2008;75(2):156-187.
- Schwarze M, Reese S. A reduced integration solid-shell finite element based on the EAS and the ANS concept – Geometrically linear problems. *Int J Numer Methods Eng*. 2009;80(10):1322-1355.
- Schwarze M, Vladimirov IN, Reese S. Sheet metal forming and springback simulation by means of a new reduced integration solid-shell finite element technology. *Comput Methods Appl Mech Eng*. 2011;200(5):454-476.
- Mostafa M, Sivaselvan M, Felippa C. A solid-shell corotational element based on ANDES, ANS and EAS for geometrically nonlinear structural analysis. *Int J Numer Methods Eng*. 2013;95(2):145-180.
- Paeppegem WV, Habraken A, Degrieck J, Alves de Sousa RJ, Valente RAF, Rah KB. Optimal low-order fully integrated solid-shell elements. *Comput Mech*. 2013;51(3):309-326.
- Sulsky D, Chen Z, Schreyer H. A particle method for history-dependent materials. *Comput Methods Appl Mech Eng*. 1994;118(1):179-196.
- Zhang X, Chen Z, Liu Y. *The Material Point Method: A Continuum-Based Particle Method for Extreme Loading Cases*. Academic Press; 2016.
- Liu P, Liu Y, Zhang X. Simulation of hyper-velocity impact on double honeycomb sandwich panel and its staggered improvement with internal-structure model. *Int J Mech Mater Des*. 2016;12(2):241-254.
- Ma S, Zhang X, Qiu X. Comparison study of MPM and SPH in modeling hypervelocity impact problems. *Int J Impact Eng*. 2009;36(2):272-282.
- Gong W, Liu Y, Zhang X, Ma H. Numerical investigation on dynamical response of aluminum foam subject to hypervelocity impact with material point method. *CMES Comput Model Eng Sci*. 2012;83(5):527-545.

16. Huang P, Zhang X, Ma S, Wang H. Shared memory OpenMP parallelization of explicit MPM and its application to hypervelocity impact. *CMES Comput Model Eng Sci.* 2008;38(2):119-148.
17. Huang P, Zhang X, Ma S, Huang X. Contact algorithms for the material point method in impact and penetration simulation. *Int J Numer Methods Eng.* 2011;85(4):498-517.
18. Ma Z, Zhang X, Huang P. An object-oriented MPM framework for simulation of large deformation and contact of numerous grains. *CMES Comput Model Eng Sci.* 2010;55(1):61-87.
19. Tan H, Nairn JA. Hierarchical, adaptive, material point method for dynamic energy release rate calculations. *Comput Methods Appl Mech Eng.* 2002;191(19-20):2123-2137.
20. Liang Y, Chandra B, Soga K. Shear band evolution and post-failure simulation by the extended material point method (XMPM) with localization detection and frictional self-contact. *Comput Methods Appl Mech Eng.* 2022;390:114530.
21. Cheon YJ, Kim HG. An adaptive material point method coupled with a phase-field fracture model for brittle materials. *Int J Numer Methods Eng.* 2019;120(8):987-1010.
22. Hu Z, Zhang H, Zheng Y, Ye H. Phase-field implicit material point method with the convected particle domain interpolation for brittle-ductile failure transition in geomaterials involving finite deformation. *Comput Methods Appl Mech Eng.* 2022;390:114420.
23. York A, Sulsky D, Schreyer H. Fluid-membrane interaction based on the material point method. *Int J Numer Methods Eng.* 2000;48(6):901-924.
24. Gilmanov A, Acharya S. A hybrid immersed boundary and material point method for simulating 3D fluid-structure interaction problems. *Int J Numer Methods Fluids.* 2008;56(12):2151-2177.
25. Li J, Hamamoto Y, Liu Y, Zhang X. Sloshing impact simulation with material point method and its experimental validations. *Comput Fluids.* 2014;103:86-99.
26. Liu Y, Ye H, Zhang H, Zheng Y. Coupling lattice Boltzmann and material point method for fluid-solid interaction problems involving massive deformation. *Int J Numer Methods Eng.* 2020;121(24):5546-5567.
27. Bardenhagen SG, Kober EM. The generalized interpolation material point method. *CMES Comput Model Eng Sci.* 2004;5(6):477-495.
28. Wallstedt PC, Guilkey J. An evaluation of explicit time integration schemes for use with the generalized interpolation material point method. *J Comput Phys.* 2008;227(22):9628-9642.
29. Steffen M, Kirby RM, Berzins M. Analysis and reduction of quadrature errors in the material point method (MPM). *Int J Numer Methods Eng.* 2008;76(6):922-948.
30. Zhang DZ, Ma X, Giguere PT. Material point method enhanced by modified gradient of shape function. *J Comput Phys.* 2011;230(16):6379-6398.
31. Sadeghirad A, Brannon RM, Burghardt J. A convected particle domain interpolation technique to extend applicability of the material point method for problems involving massive deformations. *Int J Numer Methods Eng.* 2011;86(12):1435-1456.
32. Sadeghirad A, Brannon R, Guilkey J. Second-order convected particle domain interpolation (CPDI2) with enrichment for weak discontinuities at material interfaces. *Int J Numer Methods Eng.* 2013;95(11):928-952.
33. Liang Y, Zhang X, Liu Y. An efficient staggered grid material point method. *Comput Methods Appl Mech Eng.* 2019;352:85-109.
34. Gingold RA, Monaghan JJ. Smoothed particle hydrodynamics: Theory and application to non-spherical stars. *Mon Not R Astron Soc.* 1977;181(2):375-389.
35. Maurel B, Combescure A. An SPH shell formulation for plasticity and fracture analysis in explicit dynamics. *Int J Numer Methods Eng.* 2008;76(7):949-971.
36. Belytschko T, Lu YY, Gu L. Element-free Galerkin methods. *Int J Numer Methods Eng.* 1994;37(2):229-256.
37. Krysl P, Belytschko T. Analysis of thin shells by the element-free Galerkin method. *Int J Solids Struct.* 1996;33(20):3057-3080.
38. Wang D, Chen JS. Locking-free stabilized conforming nodal integration for meshfree Mindlin-Reissner plate formulation. *Comput Methods Appl Mech Eng.* 2004;193(12):1065-1083.
39. Chen JS, Pan C, Wu CT, Liu WK. Reproducing kernel particle methods for large deformation analysis of non-linear structures. *Comput Methods Appl Mech Eng.* 1996;139(1-4):195-227.
40. Donning BM, Liu WK. Meshless methods for shear-deformable beams and plates. *Comput Methods Appl Mech Eng.* 1998;152(1):47-71.
41. Peng YX, Zhang AM, Ming FR. A thick shell model based on reproducing kernel particle method and its application in geometrically nonlinear analysis. *Comput Mech.* 2018;62(3):309-321.
42. Peng YX, Zhang AM, Ming FR. A 3D meshfree crack propagation algorithm for the dynamic fracture in arbitrary curved shell. *Comput Methods Appl Mech Eng.* 2020;367:113139.
43. Silling S. Reformulation of elasticity theory for discontinuities and long-range forces. *J Mech Phys Solids.* 2000;48(1):175-209.
44. Zhang Q, Li S, Zhang AM, Peng Y, Yan J. A peridynamic Reissner-Mindlin shell theory. *Int J Numer Methods Eng.* 2021;122(1):122-147.
45. Yang P, Liu Y, Zhang X, Zhou X, Zhao Y. Simulation of fragmentation with material point method based on Gurson model and random failure. *CMES Comput Model Eng Sci.* 2012;85(3):207.
46. Chen ZP, Zhang X, Qiu XM, Liu Y. A frictional contact algorithm for implicit material point method. *Comput Methods Appl Mech Eng.* 2017;321:124-144.
47. de Vaucorbeil A, Nguyen VP. Modelling contacts with a total Lagrangian material point method. *Comput Methods Appl Mech Eng.* 2021;373:113503.
48. Kan L, Zhang X. An immersed MMALE material point method for FSI problems with structure fracturing. *Comput Methods Appl Mech Eng.* 2022;396:115099.

49. Ni R, Li J, Zhang X, Zhou X, Cui X. An immersed boundary-material point method for shock-structure interaction and dynamic fracture. *J Comput Phys*. 2022;470:111558.
50. Belytschko T, Liu W, Moran B. *Nonlinear Finite Elements for Continua and Structures*. John Wiley and Sons Ltd.; 2000.
51. Nguyen VP, Nguyen CT, Rabczuk T, Natarajan S. On a family of convected particle domain interpolations in the material point method. *Finite Elem Anal Des*. 2017;126:50-64.
52. Guo Q, Han X, Fu C, Gast T, Tamstorf R, Teran J. A material point method for thin shells with frictional contact. *ACM Trans Graph*. 2018;37(4):1-15.
53. Kang J, Homel MA, Herbold EB. Beam elements with frictional contact in the material point method. *Int J Numer Methods Eng*. 2022;123(4):1013-1035.
54. Hughes T, Tezduyar T. Finite elements based upon mindlin plate theory with particular reference to the four-node bilinear isoparametric element. *J Appl Mech*. 1981;48:587-596.
55. Dvorkin E, Bathe K. A Continuum mechanics based four-node shell element for general nonlinear analysis. *Eng Comput*. 1984;1:77-88.
56. Macneal RH. A theorem regarding the locking of tapered four-noded membrane elements. *Int J Numer Methods Eng*. 1987;24(9):1793-1799.
57. Sze KY, Yao LQ. A hybrid stress ANS solid-shell element and its generalization for smart structure modelling. Part I – solid-shell element formulation. *Int J Numer Methods Eng*. 2000;48(4):545-564.
58. Simo JC, Rifai MS. A class of mixed assumed strain methods and the method of incompatible modes. *Int J Numer Methods Eng*. 1990;29(8):1595-1638.
59. Simo J, Armero F, Taylor R. Improved versions of assumed enhanced strain tri-linear elements for 3D finite deformation problems. *Comput Methods Appl Mech Eng*. 1993;110(3):359-386.
60. Lian YP, Zhang X, Liu Y. Coupling of finite element method with material point method by local multi-mesh contact method. *Comput Methods Appl Mech Eng*. 2011;200:3482-3494.
61. Hut P, Makino J, Mcmillan S. Building a better leapfrog. *Astrophys J*. 1995;443(2):L93-L96.
62. Ni R, Zhang X. A precise critical time step formula for the explicit material point method. *Int J Numer Methods Eng*. 2020;121:4989-5016.
63. Bardenhagen SG, Brackbill JU, Sulsky D. The material-point method for granular materials. *Comput Methods Appl Mech Eng*. 2000;187(3-4):529-541.
64. Chen Z, Qiu X, Zhang X, Lian Y. Improved coupling of finite element method with material point method based on a particle-to-surface contact algorithm. *Comput Methods Appl Mech Eng*. 2015;293:1-19.
65. Idelsohn SR, Marti J, Limache A, Onate E. Unified Lagrangian formulation for elastic solids and incompressible fluids: Application to fluid-structure interaction problems via the PFEM. *Comput Methods Appl Mech Eng*. 2008;197:1762-1776.
66. Walhorn E, Kolke A, Hubner B, Dinkler D. Fluid-structure coupling within a monolithic model involving free surface flows. *Comput Struct*. 2005;83(25-26):2100-2111.
67. Seo S, Min O, Lee J. Application of an improved contact algorithm for penetration analysis in SPH. *Int J Impact Eng*. 2008;35(6):578-588.
68. De Vuyst T, Vignjevic R, Campbell J. Coupling between meshless and finite element methods. *Int J Impact Eng*. 2005;31(8):1054-1064.

How to cite this article: Li J, Ni R, Zeng Z, Zhang X. An efficient solid shell material point method for large deformation of thin structures. *Int J Numer Methods Eng*. 2023;1-29. doi: 10.1002/nme.7359